A Black-Box Quantum Model for Superconducting Traveling-Wave Parametric Amplifiers

Michael Haider, *Member, IEEE*

***Abstract*— Superconducting quantum computing is at the forefront of demonstrating quantum advantages for revolutionary applications in science and technology. One key component for the readout of qubit state information is given by superconducting traveling-wave parametric amplifiers (TWPAs) due to their low power dissipation and unprecedented quantum-limited noise performance. This work presents a black-box circuit quantum electrodynamic model for TWPAs with arbitrary superconducting nonlinear elements. A unified Hamiltonian description for directly pumped and flux-driven amplifiers is derived, and analytic results for the gain and the added quantum noise are presented, closely matching recent experimental realizations. We also offer an optimization strategy for nonlinear elements for large gain and low noise based on the proposed black-box quantum model. The results of this article will be helpful in the design and multitarget optimization of new and improved quantum-limited low-noise amplifiers.**

***Index Terms*— Black-box model, Josephson parametric amplifier (JPA), quantum computing, qubit readout, superconducting nonlinear asymmetric inductive element (SNAIL), superconducting quantum interference device (SQUID), traveling-wave parametric amplifier (TWPA).**

I. Introduction

QUANTUM computing using superconducting qubits gained a lot of momentum recently after the demonstration of quantum supremacy [1], [2], i.e., that a programable superconducting quantum computer can solve a given problem that no classical computer could solve in a reasonable amount of time. Despite the fact that the algorithm used for the demonstration in [1] is of little to no practical relevance, and the claim was heavily debated in the community, the achievement has kicked off a vast amount of research looking for possible applications of quantum computing in different areas of science and engineering. Promising engineering applications have been found in antenna simulations, where quantum algorithms based on the quantum Fourier transform can be applied to predict power patterns of phased-array antennas [3]. A different approach, also in the field of antenna engineering, was presented in [4], where quantum annealing is used to optimize reconfigurable intelligent surfaces by recasting the problem of finding binary reflection patterns of a pixelated metasurface into the problem of finding the ground state of an equivalent Ising Hamiltonian. Both results are remarkable in the sense that the realization of practical short-term quantum advantage is currently mainly expected in the field of analog quantum simulations [5], where suitable quantum experiments model the properties of microscopic particles. Exploiting the full potential of general-purpose quantum computers based on superconducting qubits, which enables breakthrough applications in the mid and long term, however, requires further technological advances in quantum error correction and qubit readout [6].

In superconducting quantum computing, the qubit state is typically probed by a quantum nondemolition measurement of the state-dependent dispersive shift in the readout resonator's resonance frequency [7], [8], [9]. There, the qubit state is inferred by measuring the transmission of ultralow-power microwave signals [10], where the readout fidelity is limited by the signal-to-noise ratio (SNR) of the amplifier chain and the prohibitively short coherence time of the qubits [11]. Hence, the SNR of the amplifier chain must be as large as possible, i.e., quantum-limited [12] noise performance of the first-stage amplifier is critical for high-fidelity single-shot readouts of quantum information [10]. However, the relatively large noise temperature [13] and the limited cooling power budget in the lowest temperature stage of a dilution refrigerator [14] prohibit the use of cryogenic microwave amplifiers based on high-electron-mobility transistors (HEMTs). As an alternative, superconducting Josephson parametric amplifiers (JPAs) [15], [16], where the amplification is accomplished by nonlinear mixing of the input signal with a strong coherent pump field, allow for a reasonably large gain with very little power dissipation and superior noise performance [17]. Hence, they are nowadays commonly used as first-stage amplifiers in the readout of superconducting qubits [18], [19], [20], [21], [22]. For large gain, a single Josephson junction is typically coupled to a microwave resonator, where the amplifier is operated in reflection mode, neccessitating the use of a bulky circulator [14]. The resonant amplification, however, limits the gain bandwidth, and bulky circulators are prohibitive in terms of fridge space for scaled-up many-qubit quantum computers. Larger bandwidth and transmission-mode operation can be achieved using traveling-wave parametric amplifiers (TWPAs) [14], [23], [24], [25], where hundreds or even thousands of Josephson nonlinear elements are embedded within a microwave transmission line. It has been shown that these devices can be operated in the three-wave-mixing (3WM) and four-wave-mixing (4WM) regimes

Manuscript received 31 August 2023; revised 7 December 2023; accepted 17 December 2023. Date of publication 9 January 2024; date of current version 4 April 2024. This work was supported in part by the Munich Quantum Valley through the Bavarian State Government from the Hightech Agenda Bayern Plus.

The author is with the TUM School of Computation, Information and Technology, Technical University of Munich, 85748 Garching, Germany (e-mail: michael.haider@tum.de).

Color versions of one or more figures in this article are available at https://doi.org/10.1109/TMTT.2023.3345641.

Digital Object Identifier 10.1109/TMTT.2023.3345641

© 2024 The Authors. This work is licensed under a Creative Commons Attribution 4.0 License.
For more information, see https://creativecommons.org/licenses/by/4.0/

using specialized Josephson nonlinear elements [26], [27]. Although the nonlinear elements embedded within the TWPA transmission line sections become increasingly complex [28], the underlying wave-mixing mechanisms remain the same. Thus, within this article, we propose a unified realization-agnostic circuit quantum model [22], [29] for TWPAs, where the nonlinear elements are treated as black boxes. Also, the means of deriving the respective nonlinear device coefficients up to the third nonlinear order are outlined in the following [30]. This allows us to study the underlying mechanisms of parametric amplification, as well as detrimental phase-modulation and intermodal mixing effects, regardless of the actual physical device realization, conceivably leading to better devices in the future. In particular, parametric studies for device optimization will benefit from a full quantum model with analytic solutions for the gain and added quantum fluctuations in a TWPA.

This article is structured as follows. First, we introduce a unit cell model of a dissipative-dispersive nonlinear transmission line featuring periodically embedded black-box Josephson nonlinear elements in Section II. In this section, we also distinguish between directly pumped TWPAs, where a strong coherent pump tone is supplied to the same input port as the weak signal that is to be amplified, and flux-driven TWPAs, where a time-dependent modulation of the linear Josephson inductance is used for parametric amplification [27]. Section III introduces a general description for directly pumped and flux-driven Josephson nonlinear elements with arbitrary junction topology by expanding the potential energy stored in the elements up to the fourth nonlinear order. It is later shown that this description can be used to uniformly describe different existing junction topologies, such as RF [26] and dc-SQUIDs [27], as well as superconducting nonlinear asymmetric inductive elements (SNAILs) [31]. Also, Bi-SQUID-based TWPAs have been reported in the literature [32]. We introduce a third-order black-box nonlinear quantum model for TWPAs with arbitrary junction topologies in Section IV, which constitutes the central part of this article. Finally, we apply our proposed black-box quantum model to existing TWPA designs reported in the literature and show our results on the gain profile and added noise in Section V. Due to the structure-agnostic formulation of our model, it is ideally suited for device parameter optimization, which is also discussed in this section.

II. Nonlinear Transmission Line

We consider a matched 50Ω coplanar microwave transmission line on a lossy substrate material. The transmission line is periodically loaded with nonlinear elements that perform the amplifying wave-mixing operations. The superconducting nonlinear elements are formed by more or less complex arrangements of Josephson junctions, which are manufactured by sophisticated multistep evaporation processes (e.g., Al/AlO_x/Al, or Nb/Al-AlO_x/Nb, typically on silicon substrates with SiO_2 passivation layers) [33]. For the moment, we disregard the internal structure and physical mechanisms of the nonlinear elements, i.e., the nonlinearities are treated as a black box, described by a given current-phase relation $i(\varphi)$.

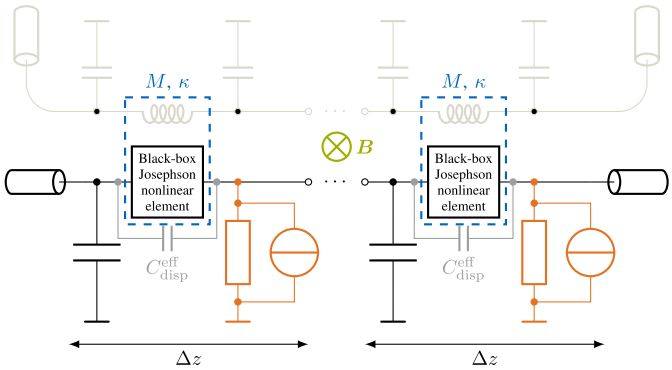

Fig. 1. Circuit representation of a TWPA with a black-box Josephson nonlinear element. The circuit model consists of N identical unit cells of length Δz. A flux bias is given by the external magnetic field $\boldsymbol{B}$. Substrate losses and noise are included in our model (orange). The ivory-colored flux–coupled (blue) transmission line represents an optional pumping mechanism for flux-driven TWPAs.

The main goal of this article is to establish a nonlinear quantum model for parametric amplification in superconducting TWPA transmission lines up to the third nonlinear order. Parametric amplification is a wave-mixing process in which energy is converted from a strong, coherent pump tone into a weak input signal to be amplified. Due to energy conservation, the process also creates another mode, the so-called idler field. In a traditional microwave amplifier, e.g., based on HEMTs, amplification is achieved by coherent modulation of a resistive channel. This adds losses, and due to the dissipation-fluctuation theorem [34], also noise to the system. In contrast, parametric amplification relies on a wave-mixing process due to a second- or third-order nonlinearity without adding additional thermal noise contributions. Although the system is assumed to be superconducting, i.e., there are no Ohmic losses along the transmission line, there are still losses and associated noise due to imperfect substrate isolation [35].

For the formulation of a black-box quantum model of distributed parametric amplification in superconducting transmission lines, we consider the unit cell, depicted in Fig. 1. A continuous coplanar transmission line can be analyzed by considering an infinitesimal line segment in terms of an equivalent circuit featuring a linear inductance per unit length, a ground capacitance per unit length, and a resistor modeling substrate losses [36]. In our unit-cell model, we neglect the series resistance, as we assume the transmission line to be superconducting, and we absorb the linear line inductance into the nonlinear black box. Additionally, we introduce a dispersion capacitor across the black-box Josephson nonlinear elements, which models the intrinsic junction capacitances. Our unit cell has a finite length Δz, given by the distance between the nonlinear elements (in the order of some 10 μm), which is, however, much smaller than the operation wavelength between 3 and 10 GHz. This means that a continuous treatment for the discrete element structure is a reasonably good approximation [37].

A. Direct Pumping

In a TWPA, a strong pump signal needs to be supplied to the nonlinear elements for efficient wave-mixing interactions.

Typically, the pump is incident at the same input port as the weak signal to be amplified. In this case, a directional coupler is needed to inject a high-power monochromatic pump tone [14]. Since the gain of a TWPA is proportional to the pump amplitude, a considerable pump power is desirable in many applications. However, the maximum pump amplitude is limited by the critical current of the Josephson elements along the transmission line. The critical current is the maximum supercurrent that can flow across the barrier of a Josephson element and depends on the junction geometry. While propagating through the nonlinear transmission line, the pump wave experiences self- and cross-phase modulation (XPM) due to the nonlinear elements.

B. Flux-Driven TWPAs

Some of the shortcomings with directly pumped TWPAs, where the pump wave is provided at the input port of the amplifier, can be overcome by considering flux-driven devices. A flux-driven TWPA is operated in a regime where the intrinsic Josephson nonlinearity is no longer used for wave-mixing interactions. Instead, parametric amplification is achieved by a time-varying modulation of the linear Josephson inductance [27]. The modulation of the linear part of the Josephson inductance arises from an additional time-varying magnetic flux threading of the nonlinear element. Hence, in a flux-driven TWPA, the nonlinear element must be formed by a loop-like geometric structure that allows for external pumping by an additional flux-coupled transmission line in close vicinity, carrying the strong microwave pump tone. Here, the pump amplitude is not limited by the critical current and is not subjected to self-phase modulation (SPM) since the pump wave travels in an independent weakly coupled linear flux line. The weakly coupled external flux line is depicted in ivory color in Fig. 1. It is, however, not necessary for parametric amplification if the pump wave is provided directly at the input port using a directional coupler. Notably, it should be mentioned that external pumping requires different design considerations for the final implementation of a TWPA [27], [32]. The operation point of a given Josephson nonlinear element with a loop-like geometry can be controlled by an external magnetic field $\boldsymbol{B}$, which causes a constant flux Φ_B in the loop. Alternatively, a constant current i_0 that is impressed along the transmission line using, e.g., a bias-tee, can alter the current–phase relation, respectively [38].

III. Models for Josephson Nonlinear Elements

In general, a Josephson nonlinear element is an inductive one port, described by a nonlinear current–phase relation $i(\varphi)$, where φ is the quantum phase difference of the superconducting wavefunctions at both contacts. The phase difference is related to the magnetic flux $\Delta\Phi_\mathrm{J}$ across the Josephson junction by $\varphi = \Delta\Phi_\mathrm{J}/\varphi_0$, where $\varphi_0 = \hbar/2e$ is the reduced magnetic flux quantum, given by the reduced Planck constant $\hbar = h/2\pi$ divided by two times the unit charge e. Interpreting the Josephson flux $\Delta\Phi_\mathrm{J} = \varphi_0\varphi$ as a space-like quantity in a Hamiltonian treatment, the potential energy stored in a single Josephson nonlinear element is given by

$$U(\varphi) = \varphi_0 \int_{\varphi^*}^{\varphi} i(\varphi')\mathrm{d}\varphi' \tag{1}$$

given a current–phase relation $i(\varphi)$. For an arbitrary current–phase relation, with an operation point selected by an external bias field $\boldsymbol{B}$, there might be a non-zero steady-state flux φ^*, determined by $i(\varphi^*) = 0$ with minimum potential energy. One would measure this flux without an external current through the junction, just due to the external flux threading. We can perform a Taylor expansion of the current–phase relation $i(\varphi)$ around the steady-state flux φ^*, i.e.,

$$\begin{aligned} i(\varphi) = {} & \left.\frac{\mathrm{d}i(\varphi)}{\mathrm{d}\varphi}\right|_{\varphi=\varphi^*}(\varphi-\varphi^*) + \frac{1}{2}\left.\frac{\mathrm{d}^2 i(\varphi)}{\mathrm{d}\varphi^2}\right|_{\varphi=\varphi^*}(\varphi-\varphi^*)^2 \\ & + \frac{1}{6}\left.\frac{\mathrm{d}^3 i(\varphi)}{\mathrm{d}\varphi^3}\right|_{\varphi=\varphi^*}(\varphi-\varphi^*)^3 + \mathcal{O}(\varphi^4). \end{aligned} \tag{2}$$

Replacing the current–phase relation in (1) by the Taylor expansion in (2), and performing the integration over the resulting polynomial yields [30]

$$\begin{aligned} \frac{U(\varphi)}{E_\mathrm{J}} \approx {} & \underbrace{\frac{1}{2I_\mathrm{c}}\left.\frac{\mathrm{d}i(\varphi)}{\mathrm{d}\varphi}\right|_{\varphi=\varphi^*}}_{c_2}\left(\varphi-\varphi^*\right)^2 \\ & + \underbrace{\frac{1}{6I_\mathrm{c}}\left.\frac{\mathrm{d}^2 i(\varphi)}{\mathrm{d}\varphi^2}\right|_{\varphi=\varphi^*}}_{c_3}\left(\varphi-\varphi^*\right)^3 \\ & + \underbrace{\frac{1}{24I_\mathrm{c}}\left.\frac{\mathrm{d}^3 i(\varphi)}{\mathrm{d}\varphi^3}\right|_{\varphi=\varphi^*}}_{c_4}\left(\varphi-\varphi^*\right)^4 \end{aligned} \tag{3}$$

with the Josephson energy $E_\mathrm{J} = \varphi_0 I_\mathrm{c}$. The coefficients c_2, c_3, and c_4 describe the Josephson nonlinear element up to the third order. In the following, we want to establish a third-order black-box quantum model based on a Hamiltonian explicitly depending on these coefficients.

For flux-driven TWPAs, the intrinsic nonlinearity of the Josephson elements is no longer used for the wave-mixing interactions [27]. Due to the absence of a strong pump mode propagating along the nonlinear transmission line, the system is not driven into nonlinear behavior. By contrast, a time-varying modulation of the linear inductance of the respective black-box element is used in a first-order approximation. Hence, the potential energy from (1) can be rewritten as

$$\begin{aligned} U(\varphi) &= \varphi_0 \int_{\varphi^*}^{\varphi} i(\varphi', \varphi_\mathrm{ext})\mathrm{d}\varphi' \\ &\approx \frac{\varphi_0}{2}\left.\frac{\partial i(\varphi, \varphi_\mathrm{ext})}{\partial\varphi}\right|_{\varphi=\varphi^*}\left(\varphi-\varphi^*\right)^2 \end{aligned} \tag{4}$$

where $\varphi_\mathrm{ext} = \varphi_\mathrm{B} + \varphi_\mathrm{ac}$ is the external flux threading given by a large constant bias phase φ_B and a time-varying pump phase φ_ac with $\varphi_\mathrm{ac} \ll \varphi_\mathrm{B}$. Hence, in the flux-driven case, we perform another Taylor expansion of (4) with respect to φ_ext around φ_B,

i.e.,

$$\frac{U(\varphi)}{E_{\mathrm{J}}} \approx \underbrace{\frac{1}{2I_{\mathrm{c}}}\frac{\partial i(\varphi,\varphi_{\mathrm{ext}})}{\partial\varphi}\bigg|_{\substack{\varphi=\varphi^*,\\ \varphi_{\mathrm{ext}}=\varphi_{\mathrm{B}}}}}_{c_2}(\varphi-\varphi^*)^2 + \underbrace{\frac{1}{2I_{\mathrm{c}}}\frac{\partial^2 i(\varphi,\varphi_{\mathrm{ext}})}{\partial\varphi\partial\varphi_{\mathrm{ext}}}\bigg|_{\substack{\varphi=\varphi^*,\\ \varphi_{\mathrm{ext}}=\varphi_{\mathrm{B}}}}}_{c_3}\varphi_{\mathrm{ac}}(\varphi-\varphi^*)^2 + \underbrace{\frac{1}{4I_{\mathrm{c}}}\frac{\partial^3 i(\varphi,\varphi_{\mathrm{ext}})}{\partial\varphi\partial\varphi_{\mathrm{ext}}^2}\bigg|_{\substack{\varphi=\varphi^*,\\ \varphi_{\mathrm{ext}}=\varphi_{\mathrm{B}}}}}_{c_4}\varphi_{\mathrm{ac}}^2(\varphi-\varphi^*)^2 \quad (5)$$

where we identified $\varphi_{\mathrm{ac}} = \varphi_{\mathrm{ext}} - \varphi_{\mathrm{B}}$.

Overall, the coefficients c_2, c_3, and c_4, describing a black-box Josephson nonlinear element up to the third order, are given by

$$c_2 = \begin{cases} \dfrac{1}{2I_{\mathrm{c}}}\dfrac{\mathrm{d}i(\varphi)}{\mathrm{d}\varphi}\bigg|_{\varphi=\varphi^*}, & \text{for direct pumping} \\ \dfrac{1}{2I_{\mathrm{c}}}\dfrac{\partial i(\varphi,\varphi_{\mathrm{ext}})}{\partial\varphi}\bigg|_{\substack{\varphi=\varphi^*,\\ \varphi_{\mathrm{ext}}=\varphi_{\mathrm{B}}}}, & \text{for flux-driven TWPAs} \end{cases} \quad (6)$$

$$c_3 = \begin{cases} \dfrac{1}{6I_{\mathrm{c}}}\dfrac{\mathrm{d}^2 i(\varphi)}{\mathrm{d}\varphi^2}\bigg|_{\varphi=\varphi^*}, & \text{for direct pumping} \\ \dfrac{1}{4I_{\mathrm{c}}}\dfrac{\partial^3 i(\varphi,\varphi_{\mathrm{ext}})}{\partial\varphi\partial\varphi_{\mathrm{ext}}^2}\bigg|_{\substack{\varphi=\varphi^*,\\ \varphi_{\mathrm{ext}}=\varphi_{\mathrm{B}}}}, & \text{for flux-driven TWPAs} \end{cases} \quad (7)$$

$$c_4 = \begin{cases} \dfrac{1}{24I_{\mathrm{c}}}\dfrac{\mathrm{d}^3 i(\varphi)}{\mathrm{d}\varphi^3}\bigg|_{\varphi=\varphi^*}, & \text{for direct pumping} \\ \dfrac{1}{2I_{\mathrm{c}}}\dfrac{\partial^2 i(\varphi,\varphi_{\mathrm{ext}})}{\partial\varphi\partial\varphi_{\mathrm{ext}}}\bigg|_{\substack{\varphi=\varphi^*,\\ \varphi_{\mathrm{ext}}=\varphi_{\mathrm{B}}}}, & \text{for flux-driven TWPAs.} \end{cases} \quad (8)$$

For any given element with a current–phase relation $i(\varphi)$, these coefficients can be easily extracted and fed into our quantum model for parametric amplification. Possible realizations for the black-box Josephson nonlinear elements are given in Fig. 2. The nonlinear coefficients for some of these structures are explicitly evaluated in [28], [31], [39], [40], [41], and [42].

IV. Black-Box Quantum Model

Independent of the actual physical realization, we now want to construct a quantum model of parametric amplification in superconducting directly pumped and flux-driven TWPAs. The parametric gain in the quantum model will only depend on the nonlinear parameters c_2, c_3, and c_4 of the black-box Josephson nonlinear element. Additional degrees of freedom are the respective design choices for the transmission line parameters. The black-box nonlinear element, internally composed of Josephson junctions, will behave like a nonlinear inductor. Expanding the system up to linear order yields the effective linear Josephson inductance of the element, which is given as

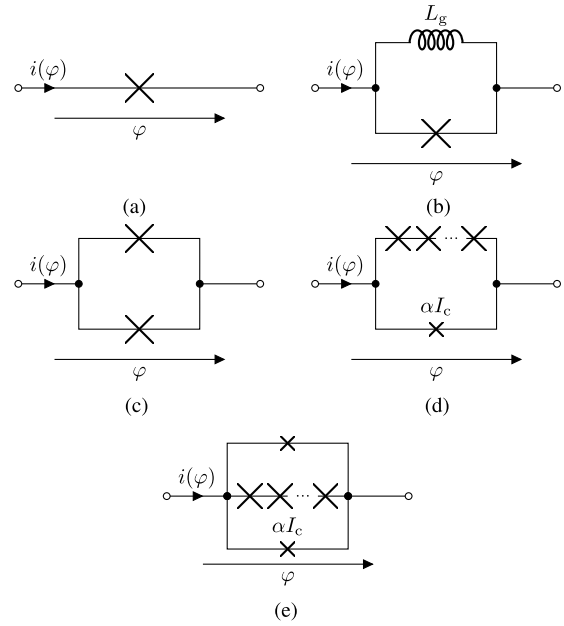

Fig. 2. Circuit representation of (a) single junction, (b) RF-SQUID, (c) dc-SQUID, (d) and SNAIL, and (e) gradiometric SNAIL. The RF-SQUID consists of a single Josephson junction embedded in a loop-like geometry with a geometric inductance L_{g}. A dc-SQUID comprises two identical Josephson junctions forming a ring structure. In a SNAIL, n large junctions and a single small junction with a critical current αI_{c}, where I_{c} is the critical current of the large junctions and α is the asymmetry ratio, form a loop-like geometry. A gradiometric SNAIL is additionally shorted by another small junction, forming a second loop.

a function of c_2 by

$$L_{\mathrm{J},0} = \frac{\varphi_0}{2I_{\mathrm{c}}}\frac{1}{c_2}. \quad (9)$$

Hence, the effective linear inductance of the element is inversely proportional to the parameter c_2. In order to investigate parametric amplification of a signal propagating through the amplifier's nonlinear transmission line, we need to model the incoming weak photon field at the input of the amplifier as a traveling-wave mode. Traveling-wave amplitudes in a dispersionless transmission line exhibit space–time translation invariance [43]. Thus, a single spatial or temporal dependence can describe a wave amplitude. In the modeling of TWPAs, one typically considers only right-propagating waves. We choose to describe our system in terms of time-dependent wave amplitudes that evolve in a co-propagating reference timeframe [22]. In the case of a dispersive transmission line, each mode travels at a slightly different velocity. Hence, the velocity of the co-propagating timeframe would be different for each mode. This must be properly accounted for whenever modes of different frequencies are coupled in the nonlinear elements. To circumvent this problem, we introduce a fixed reference timeframe that moves with a constant velocity given by $(\Delta z/L_{\mathrm{J},0}C')^{1/2}$, and introduce a frequency-dependent, dimensionless dispersion factor $\Lambda(\omega)$ to compensate for different propagation speeds, i.e., to translate between the individual timeframes. The fixed reference velocity used here corresponds to a linear lossless transmission line that would have the same inductance per unit length $L_{\mathrm{J},0}/\Delta z$ and the same capacitance per unit length C' as the nonlinear

transmission line, featuring our black-box loadings. The dimensionless dispersion factor as a function of c_2 is given by

$$\Lambda(\omega) = \frac{1+\sqrt{1+\frac{1}{\omega^2 R^2 C'^2 \Delta z^2}}}{2\left(1-\frac{\varphi_0 \omega^2 C_{\text{disp}}^{\text{eff}}}{2 I_c c_2}\right)} \approx \frac{2 I_c c_2}{2 I_c c_2 - \varphi_0 \omega^2 C_{\text{disp}}^{\text{eff}}} \quad (10)$$

and includes dispersion due to the effective capacitance across the black-box elements from Fig. 1, as well as possible substrate losses in terms of the substrate resistance R. As the substrate resistance is typically huge, it can be safely neglected here, yielding the approximate dispersion factor on the right-hand side of (10).

The effective magnetic flux wave across the Josephson nonlinear element $\hat{\varphi}_{\text{eff}} = \hat{\varphi} - \varphi^*$, which represents the traveling electromagnetic field along the nonlinear transmission line, can be described by the continuous mode operator [22], [44]

$$\hat{\varphi}_{\text{eff}} = \frac{\Delta z}{\sqrt{2\pi}} \int_0^\infty \left[\sqrt{\frac{\hbar k(\omega)^3}{2 C' \omega^2 \varphi_0^2}} \hat{a}_\omega e^{ik(\omega)z - i\omega t} + \text{H. c.} \right] d\omega \quad (11)$$

with the dispersion relation

$$k(\omega) = \omega \sqrt{\frac{\varphi_0 C' \Lambda(\omega)}{2 I_c c_2 \Delta z}}. \quad (12)$$

To investigate the field's quantum nature, a circuit quantum electrodynamic treatment is necessary, where the field in (11) is expanded into Bosonic creation and annihilation operators, $\hat{a}_\omega^\dagger$ and $\hat{a}_\omega$, respectively. This is similar to an expansion of the traveling-wave flux field into 1-D plane waves, where the plane wave amplitudes are given by harmonic oscillators, representing a quantum field mode with frequency ω. The annihilation operator $\hat{a}_\omega$ and the corresponding creation operator $\hat{a}_\omega^\dagger$ fulfill the Bosonic commutator relation $[\hat{a}_\omega, \hat{a}_{\omega'}^\dagger] = \hat{a}_\omega \hat{a}_{\omega'}^\dagger - \hat{a}_{\omega'}^\dagger \hat{a}_\omega = \delta(\omega - \omega')$. Hence, the creation operator $\hat{a}_\omega^\dagger$ and the annihilation operator $\hat{a}_\omega$ together describe the spatiotemporal evolution of the effective phase operator $\hat{\varphi}_{\text{eff}}$, and thus, of the quantized electromagnetic field in the transmission line. An introduction to electromagnetic circuit quantization for microwave engineers can be found in [45], while some key concepts are also outlined in [46].

It makes sense to decompose the mode spectrum at the input of the amplifier into a weak photon field with annihilation operator $\hat{a}_\omega$, that is to be amplified, and a strong coherent pump tone $\hat{a}_{\Omega_p}$. The pump tone is supplied directly to the input using a directional coupler or flux-coupled to the amplifier via an external pump line.

For constructing the Hamiltonian, we must again distinguish between directly pumped and flux-driven TWPAs. Expressing the potential energy from (3) in terms of a quantum operator $\hat{\varphi}_{\text{eff}}$ and adding the kinetic energy in the dispersion capacitor $C_{\text{disp}}^{\text{eff}}$ and in the ground capacitor $\Delta z C'$ yields the total system Hamiltonian $\hat{H}$ for a directly pumped TWPA without considering losses

$$\hat{H} = \frac{1}{\Delta z} \int_0^x \left[E_J c_2 \hat{\varphi}_{\text{eff}}^2 + E_J c_3 \hat{\varphi}_{\text{eff}}^3 + E_J c_4 \hat{\varphi}_{\text{eff}}^4 + \frac{\varphi_0^2}{2} C_{\text{disp}}^{\text{eff}} \left(\frac{\partial \hat{\varphi}_{\text{eff}}}{\partial t} \right)^2 + \frac{1}{2 \Delta z C'} \hat{Q}^2 \right] dz. \quad (13)$$

In the case of a flux-driven TWPA, we need to express the potential energy from (5) in terms of $\hat{\varphi}_{\text{eff}}$ instead. We also need a quantum description for the flux-coupled pump field incident from the separate pump line. The operator for the quantum phase difference due to the external pump $\hat{\varphi}_{\text{ac}}$ is given by

$$\hat{\varphi}_{\text{ac}} = \frac{\kappa \Delta z}{\sqrt{2\pi}} \int_0^\infty \left[\sqrt{\frac{\hbar k(\Omega_p) k'(\Omega_p)^2}{2 C_p' \Omega_p^2 \varphi_0^2}} \hat{a}_{\Omega_p} e^{ik(\Omega_p)z - i\Omega_p t} + \text{H.c.} \right] d\Omega_p \quad (14)$$

where κ is a coupling coefficient between the external flux line and the nonlinear transmission line. The wavevector k' in the external flux line is given by the dispersion relation

$$k'(\omega) = \omega \sqrt{\frac{\varphi_0^2 C' \Lambda_p}{4 I_c^2 c_2^2 \Delta z^2 L_p'}} \quad (15)$$

with the dimensionless, frequency-independent pump-line dispersion factor Λ_p, which is equal to

$$\Lambda_p = \frac{2 I_c c_2 \Delta z C_p' L_p'}{\varphi_0 C'}. \quad (16)$$

Here, L_p' and C_p' are the inductance per unit length and capacitance per unit length of the external pump line, respectively. The Hamiltonian for a flux-driven TWPA in the nonlinear transmission line, expressed in terms of c_2, c_3, and c_4, is given by

$$\hat{H} = \frac{1}{\Delta z} \int_0^x \left[E_J c_2 \hat{\varphi}_{\text{eff}}^2 + E_J c_3 \hat{\varphi}_{\text{ac}} \hat{\varphi}_{\text{eff}}^2 + E_J c_4 \hat{\varphi}_{\text{ac}}^2 \hat{\varphi}_{\text{eff}}^2 + \frac{\varphi_0^2}{2} C_{\text{disp}}^{\text{eff}} \left(\frac{\partial \hat{\varphi}_{\text{eff}}}{\partial t} \right)^2 + \frac{1}{2 \Delta z C'} \hat{Q}^2 \right] dz \quad (17)$$

where the operators $\hat{\varphi}_{\text{eff}}$ and $\hat{\varphi}_{\text{ac}}$ commute, i.e., $[\hat{\varphi}_{\text{eff}}, \hat{\varphi}_{\text{ac}}] = \hat{\varphi}_{\text{eff}} \hat{\varphi}_{\text{ac}} - \hat{\varphi}_{\text{ac}} \hat{\varphi}_{\text{eff}} = 0$.

Inserting the Bosonic mode operators from (11) and (14) into the Hamiltonians (13) and (17), and neglecting nonresonant terms, unveils the underlying wave mixing mechanisms up to third order. The unperturbed linear part of the free-propagating signal and pump fields is given by the Hamiltonian $\hat{H}_0$. In both cases, the unperturbed Hamiltonian $\hat{H}_0$ is given by

$$\hat{H}_0 = \int_0^\infty \hbar \omega \hat{a}_\omega^\dagger \hat{a}_\omega d\omega + \int_0^\infty \hbar \Omega_p \hat{a}_{\Omega_p}^\dagger \hat{a}_{\Omega_p} d\Omega_p. \quad (18)$$

From the terms proportional to the nonlinear coefficient c_3 in (13) and (17), we can derive a 3WM part $\hat{H}_{3\text{WM}}$ of

the total Hamiltonian, given by

$$\hat{H}_{3\mathrm{WM}} = \int_0^\infty\int_0^\infty\int_0^\infty \left[\frac{\sqrt{\hbar^3 C'}\, f^{\Lambda}_{\Omega_\mathrm{p},\omega,\omega'}}{16 I_\mathrm{c}\sqrt{\pi^3}}\left(\frac{81\varphi_0 C'}{2 I_\mathrm{c} c_2 \Delta z}\right)^{\frac{m}{4}} \times \frac{c_3}{c_2^2}\hat{a}^\dagger_\omega \hat{a}^\dagger_{\omega'}\hat{a}_{\Omega_\mathrm{p}} \mathrm{e}^{-\mathrm{i}(\Omega_\mathrm{p}-\omega-\omega')t} \times \int_0^x \mathrm{e}^{\mathrm{i}[k(\Omega_\mathrm{p})-k(\omega)-k(\omega')]z}\mathrm{d}z + \mathrm{H.c.}\right] \times \left[\kappa\left(L'_\mathrm{p}C'_\mathrm{p}\right)^{\frac{1}{4}}\right]^{1-m} \mathrm{d}\omega\mathrm{d}\omega'\mathrm{d}\Omega_\mathrm{p}\,. \tag{19}$$

In (19) and in the following, $m \in \{0, 1\}$ is a binary selection parameter, where m equals one for the case of direct pumping and zero for external flux drive. The dispersion product $f^{\Lambda}_{\Omega_\mathrm{p},\omega,\omega'}$ can be evaluated from the general form

$$f^{\Lambda}_{\omega_1,\ldots,\omega_N} = \prod_{n=1}^{N}\sqrt{\omega_n}\,\Lambda(\omega_n)^{\frac{3}{4}}\,. \tag{20}$$

The 3WM nature of (19) becomes apparent from the operator product $\hat{a}^\dagger_\omega\hat{a}^\dagger_{\omega'}\hat{a}_{\Omega_\mathrm{p}}$, representing the annihilation of a photon in the pump mode at frequency Ω_p, and the simultaneous creation of a signal photon at frequency ω and another photon at frequency ω'.

Similarly, we obtain a 4WM part $\hat{H}_{4\mathrm{WM}}$ of the Hamiltonian from terms proportional to the nonlinear coefficient c_4. Jointly represented for internal and external pumping, the 4WM Hamiltonian is given by

$$\hat{H}_{4\mathrm{WM}} = \int_0^\infty\int_0^\infty\int_0^\infty\int_0^\infty \left[\frac{\hbar^2\sqrt{C'\Delta z}\, f^{\Lambda}_{\Omega_\mathrm{p},\Omega'_\mathrm{p},\omega,\omega'}}{32\pi^2\sqrt{2 I_\mathrm{c}^3\varphi_0}}\left(\frac{36\varphi_0 C'}{2 I_\mathrm{c} c_2 \Delta z}\right)^{\frac{m}{2}} \times \frac{c_4}{c_2^{5/2}}\hat{a}^\dagger_\omega\hat{a}^\dagger_{\omega'}\hat{a}_{\Omega_\mathrm{p}}\hat{a}_{\Omega'_\mathrm{p}} \mathrm{e}^{\mathrm{i}(\Omega_\mathrm{p}+\Omega'_\mathrm{p}-\omega-\omega')t} \times \int_0^x \mathrm{e}^{\mathrm{i}\left[k(\Omega_\mathrm{p})+k(\Omega'_\mathrm{p})-k(\omega)-k(\omega')\right]z}\mathrm{d}z + \mathrm{H.c.}\right] \times \left[\kappa^2\left(L'_\mathrm{p}C'_\mathrm{p}\right)^{\frac{1}{2}}\right]^{1-m} \mathrm{d}\omega\mathrm{d}\omega'\mathrm{d}\Omega_\mathrm{p}\mathrm{d}\Omega'_\mathrm{p} \tag{21}$$

where 4WM is due to the operator product $\hat{a}^\dagger_\omega\hat{a}^\dagger_{\omega'}\hat{a}_{\Omega_\mathrm{p}}\hat{a}_{\Omega'_\mathrm{p}}$. Here, two pump photons at frequencies Ω_p and Ω'_p are annihilated, creating a signal photon in the mode with frequency ω and an additional idler photon at frequency ω'. The interaction strength is proportional to $c_4/c_2^{5/2}$.

Depending on the desired operation mode, either (19) or (21) can be used for parametric amplification. The operation mode is selected by the frequency of the pump tone and by the respective 3WM and 4WM coupling strengths set by the nonlinear coefficients c_3 and c_4. Hence, some amplifier implementations with a suitable choice of c_3 and c_4 can be operated in either 3WM or 4WM mode, depending on the frequency Ω_p of the supplied pump tone with respect to the signal mode frequency ω.

4WM, however, also allows for other possible resonant interactions of the weak photon field and the pump drive or of the pump drive with itself. These effects are called XPM and SPM. XPM occurs due to a non-vanishing coefficient c_4 for internal and external pumping. With the binary selection parameter m, the XPM Hamiltonian is given by

$$\hat{H}_{\mathrm{XPM}} = \int_0^\infty\int_0^\infty\int_0^\infty\int_0^\infty \frac{\hbar^2\sqrt{C'\Delta z}\, f^{\Lambda}_{\Omega_\mathrm{p},\Omega'_\mathrm{p},\omega,\omega'}}{16\pi^2\sqrt{2 I_\mathrm{c}^3\varphi_0}}\left(\frac{36\varphi_0 C'}{2 I_\mathrm{c} c_2 \Delta z}\right)^{\frac{m}{2}} \times \frac{c_4}{c_2^{5/2}}\hat{a}^\dagger_\omega\hat{a}_{\omega'}\hat{a}^\dagger_{\Omega_\mathrm{p}}\hat{a}_{\Omega'_\mathrm{p}} \mathrm{e}^{\mathrm{i}(\Omega_\mathrm{p}-\Omega'_\mathrm{p}+\omega-\omega')t} \times \int_0^x \mathrm{e}^{-\mathrm{i}\left[k(\Omega_\mathrm{p})-k(\Omega'_\mathrm{p})+k(\omega)-k(\omega')\right]z}\mathrm{d}z \times \left[\kappa^2\left(L'_\mathrm{p}C'_\mathrm{p}\right)^{\frac{1}{2}}\right]^{1-m} \mathrm{d}\omega\mathrm{d}\omega'\mathrm{d}\Omega_\mathrm{p}\mathrm{d}\Omega'_\mathrm{p}\,. \tag{22}$$

The input photon field $\hat{a}_\omega$ is assumed to be very weak, i.e., in the range of just a few microwave photons. Thus, SPM of the signal mode plays a subordinate role and can be neglected. SPM of the strong pump field, however, needs to be taken into account, as the pump tone is assumed to be strong enough to drive the system into nonlinearity, at least in the case of direct pumping. In contrast to direct pumping, a pump tone propagating in an external, weakly coupled transmission line does not directly experience the black-box nonlinear elements and is thus not affected by SPM. The SPM Hamiltonian of the pump field for the case of direct pumping is then given by

$$\hat{H}_{\mathrm{SPM}} = \int_0^\infty\int_0^\infty\int_0^\infty\int_0^\infty \frac{\hbar^2\sqrt{C'\Delta z}\, f^{\Lambda}_{\Omega_\mathrm{p},\Omega'_\mathrm{p},\tilde{\Omega}_\mathrm{p},\tilde{\Omega}'_\mathrm{p}}}{64\pi^2\sqrt{2 I_\mathrm{c}^3\varphi_0}}\left(\frac{36\varphi_0 C'}{2 I_\mathrm{c} c_2 \Delta z}\right)^{\frac{1}{2}} \times \frac{c_4}{c_2^{5/2}}\hat{a}^\dagger_{\Omega_\mathrm{p}}\hat{a}_{\Omega'_\mathrm{p}}\hat{a}^\dagger_{\tilde{\Omega}_\mathrm{p}}\hat{a}_{\tilde{\Omega}'_\mathrm{p}} \mathrm{e}^{\mathrm{i}(\Omega_\mathrm{p}-\Omega'_\mathrm{p}+\tilde{\Omega}_\mathrm{p}-\tilde{\Omega}'_\mathrm{p})t} \times \int_0^x \mathrm{e}^{-\mathrm{i}\left[k(\Omega_\mathrm{p})-k(\Omega'_\mathrm{p})+k(\tilde{\Omega}_\mathrm{p})-k(\tilde{\Omega}'_\mathrm{p})\right]z}\mathrm{d}z \times \left(2^m-1\right)\mathrm{d}\Omega_\mathrm{p}\mathrm{d}\Omega'_\mathrm{p}\mathrm{d}\tilde{\Omega}_\mathrm{p}\mathrm{d}\tilde{\Omega}'_\mathrm{p}\,. \tag{23}$$

In order to model losses and noise due to the imperfect substrate isolation, we add a phenomenological heat bath [22], [35], representing an environmental photon field [47]. The distributed bath consists of an infinite number of harmonic oscillators with Bosonic creation and annihilation operators $\hat{b}_n$ and $\hat{b}^\dagger_n$. The bath field can be described by the Hamiltonian

$$\hat{H}_{\mathrm{bath}} = \sum_n \hbar\omega_n \int_0^\infty \hat{b}^\dagger_n(\omega)\hat{b}_n(\omega)\mathrm{d}\omega \tag{24}$$

where we omitted the zero-point energy. Neglecting the zero-point energy is justified, as it will not play a role in the commutator relations forming the equations of motion for the bath modes later on [47]. The heat bath is coupled to the Bosonic field modes inside the amplifier by means of phenomenological coupling constants g_n. The field-bath coupling can be described by the Hamiltonian

$$\hat{H}_{\mathrm{coupling}} = \sum_n \hbar\int_0^\infty \left[g_n(\omega)\hat{b}^\dagger_n(\omega)\hat{a}_\omega + \mathrm{H.c.}\right]\mathrm{d}\omega\,. \tag{25}$$

Note that the coupling is bidirectional, such that energy might be dissipated into the bath, but also thermally excited photons (i.e., thermal noise) can be brought back from the environment into the field mode in terms of the fluctuation-dissipation theorem [34]. Classically, this resembles a resistor, modeling the substrate losses (out-coupling into the environment), and a

noise current source, which describes thermal fluctuations (in-coupling from the environment), given by Johnson–Nyquist noise [48], [49]. Hence, the bath and bath coupling Hamiltonians complete the circuit quantum electrodynamic black-box model by describing the orange (light-gray) resistor and associated current source in Fig. 1.

Overall, we can now distinguish four different scenarios. In the first one, we have a dominant 3WM interaction with residual 4WM, operated with an appropriate pump tone, which is directly supplied to the input of the amplifier. Thus, the Hamiltonian, in this case, reads as

$$\hat{H} = \hat{H}_0 + \hat{H}_{3\mathrm{WM}} + \hat{H}_{\mathrm{XPM}} + \hat{H}_{\mathrm{SPM}} + \hat{H}_{\mathrm{bath}} + \hat{H}_{\mathrm{coupling}} \tag{26}$$

with $m = 1$. The Hamiltonian for an internally pumped device operating in the 4WM regime, on the other hand, is given by

$$\hat{H} = \hat{H}_0 + \hat{H}_{4\mathrm{WM}} + \hat{H}_{\mathrm{XPM}} + \hat{H}_{\mathrm{SPM}} + \hat{H}_{\mathrm{bath}} + \hat{H}_{\mathrm{coupling}} \tag{27}$$

with $m = 1$. In the remaining two cases, i.e., with external pumping, SPM does not play a role and is therefore not included in the total Hamiltonian. For a flux-driven TWPA with a dominant 3WM nonlinearity, the Hamiltonian is given by

$$\hat{H} = \hat{H}_0 + \hat{H}_{3\mathrm{WM}} + \hat{H}_{\mathrm{XPM}} + \hat{H}_{\mathrm{bath}} + \hat{H}_{\mathrm{coupling}} \tag{28}$$

including residual XPM effects. Similarly, the Hamiltonian for an externally pumped 4WM TWPA can be written as

$$\hat{H} = \hat{H}_0 + \hat{H}_{4\mathrm{WM}} + \hat{H}_{\mathrm{XPM}} + \hat{H}_{\mathrm{bath}} + \hat{H}_{\mathrm{coupling}}. \tag{29}$$

To get rid of the unperturbed evolution, we switch to a Heisenberg interaction picture, rotating with $\exp(\mathrm{i}\hat{H}_0 t/\hbar)$. Furthermore, we assume that the pump modes in both cases, 3WM and 4WM, are represented by strong monochromatic discrete mode operators at a single degenerate pump frequency $\Omega_\mathrm{p} = \Omega'_\mathrm{p} = \omega_\mathrm{p}$. The continuous mode pump operators $\hat{a}_{\omega_\mathrm{p}}$ can then be replaced by their discrete counterparts according to

$$\sqrt{\frac{\hbar\Omega_\mathrm{p}}{2C' v_\mathrm{ph}(\Omega_\mathrm{p})}}\hat{a}_{\Omega_\mathrm{p}} \to \sqrt{2\pi}\sqrt{\frac{\hbar\omega_\mathrm{p}}{2C' l_\mathrm{q}}}\hat{a}_\mathrm{p}\delta(\Omega_\mathrm{p} - \omega_\mathrm{p}) \tag{30}$$

with a quantization length l_q [22], [50]. The phase velocity of the pump wave is equal to $v_\mathrm{ph}(\omega) = \omega/k(\omega)$ for direct pumping and $v_\mathrm{ph}(\omega) = \omega/k'(\omega)$ in the case of an external pump.

In the asymptotic scattering limit [51], [52], the unitary time-evolution operator $\hat{U}$ of the system can be obtained in a first-order perturbation theory, neglecting time ordering [53], [54]

$$\begin{aligned}\lim_{\substack{t_0\to-\infty\\ t\to\infty}} \hat{U}(t_0, t) &= \lim_{\substack{t_0\to-\infty\\ t\to\infty}} \exp\left[-\frac{\mathrm{i}}{\hbar}\int_{t_0}^{t}\hat{H}(\tau)\mathrm{d}\tau\right] \\ &= \exp\left[-\frac{\mathrm{i}}{\hbar}\hat{K}\right].\end{aligned} \tag{31}$$

Hence, we form a propagator $\hat{K}$ in a first-order perturbation theory by integrating the desired system Hamiltonian, which is one of (26)–(29). Due to the time integral, the time-dependent complex exponentials in (19) and (21)–(23) yield Dirac delta distributions, and hence, strict requirements for the signal and idler frequencies concerning the pump tone. In the case of 3WM, the pump frequency must be equal to the sum of the signal and idler frequencies, i.e., $\omega_\mathrm{p} = \omega + \omega'$. For 4WM, on the other hand, the pump frequency must be half as large, i.e., $2\omega_\mathrm{p} = \omega + \omega'$. These requirements are a direct consequence of energy conservation and are well known in terms of the Manley–Rowe relations [55], [56].

Performing the replacement in (30) and integrating (26) or (28) over time yield a single propagator $\hat{K}$ for the 3WM Hamiltonian when making use of the resulting delta distributions. The single propagator $\hat{K}$ corresponds to internal and external pumping, depending on the binary selection parameter m. The propagator $\hat{K}$ is given by

$$\begin{aligned}\hat{K} = \int_0^\infty &\left[\frac{\sqrt{2\hbar^3 v_\mathrm{ph}(\omega_\mathrm{p})C'}\, f^{\Lambda}_{\omega_{\omega,\omega_\mathrm{p}-\omega,\omega_\mathrm{p}}}}{8I_\mathrm{c}\sqrt{l_\mathrm{q}}}\left(\frac{81\varphi_0}{2I_\mathrm{c}c_2\Delta z}\right)^{\frac{m}{4}}\right. \\ &\left.\times\frac{c_3}{c_2^2}\hat{a}_\mathrm{p}\hat{a}^\dagger_\omega\hat{a}^\dagger_{\omega_\mathrm{p}-\omega}\int_0^x \mathrm{e}^{\mathrm{i}\Delta k_{3\mathrm{WM}}z}\mathrm{d}z + \mathrm{H.c.}\right] \\ &\times\left[\kappa\left(L'_\mathrm{p}C'_\mathrm{p}\right)^{\frac{1}{4}}\right]^{1-m}\mathrm{d}\omega \\ &+\int_0^\infty \frac{\hbar^2 v_\mathrm{ph}(\omega_\mathrm{p})\sqrt{\Delta z C'}\, f^{\Lambda}_{\omega,\omega,\omega_\mathrm{p},\omega_\mathrm{p}}}{4\sqrt{2I_\mathrm{c}^3\varphi_0}\, l_\mathrm{q}}\left(\frac{36\varphi_0}{2I_\mathrm{c}c_2\Delta z}\right)^{\frac{m}{2}} \\ &\times\frac{c_4}{c_2^{5/2}}\hat{a}^\dagger_\mathrm{p}\hat{a}_\mathrm{p}\hat{a}^\dagger_\omega\hat{a}_\omega\int_0^x \mathrm{e}^{\mathrm{i}\Delta k_{\mathrm{XPM}}z}\mathrm{d}z \\ &\times\left[\kappa^2\left(L'_\mathrm{p}C'_\mathrm{p}\right)^{\frac{1}{2}}\right]^{1-m}\mathrm{d}\omega \\ &+\frac{\hbar^2 v_\mathrm{ph}(\omega_\mathrm{p})\sqrt{\Delta z C'}\, f^{\Lambda}_{\omega_\mathrm{p},\omega_\mathrm{p},\omega_\mathrm{p},\omega_\mathrm{p}}}{16\sqrt{2I_\mathrm{c}^3\varphi_0}\, l_\mathrm{q}}\left(\frac{36\varphi_0}{2I_\mathrm{c}c_2\Delta z}\right)^{\frac{1}{2}} \\ &\times\frac{c_4}{c_2^{5/2}}\hat{a}^\dagger_\mathrm{p}\hat{a}_\mathrm{p}\hat{a}^\dagger_\mathrm{p}\hat{a}_\mathrm{p}\int_0^x \mathrm{e}^{\mathrm{i}\Delta k_{\mathrm{SPM}}z}\mathrm{d}z\left(2^m - 1\right) \\ &+\int_{-\infty}^{\infty}\int_0^\infty\sum_n \hbar\omega_n\hat{b}^\dagger_n(\omega)\hat{b}_n(\omega)\mathrm{d}\omega\mathrm{d}t \\ &+\int_{-\infty}^{\infty}\int_0^\infty\sum_n \hbar\left[g_n(\omega)\hat{b}^\dagger_n(\omega)\hat{a}_\omega\mathrm{e}^{-i\omega t} + \mathrm{H.c.}\right]\mathrm{d}\omega\mathrm{d}t\,.\end{aligned} \tag{32}$$

The wavevector phase differences $\Delta k_{3\mathrm{WM}}$, Δk_{XPM}, and Δk_{SPM} in (32) are given by

$$\Delta k_{3\mathrm{WM}} = \tilde{k}(\omega_\mathrm{p}) - k(\omega) - k(\omega_\mathrm{p} - \omega) \tag{33}$$

$$\Delta k_{\mathrm{XPM}} = \tilde{k}(\omega_\mathrm{p}) - \tilde{k}(\omega_\mathrm{p}) + k(\omega) - k(\omega) = 0 \tag{34}$$

$$\Delta k_{\mathrm{SPM}} = \tilde{k}(\omega_\mathrm{p}) - \tilde{k}(\omega_\mathrm{p}) + \tilde{k}(\omega_\mathrm{p}) - \tilde{k}(\omega_\mathrm{p}) = 0 \tag{35}$$

where

$$\tilde{k}(\omega_\mathrm{p}) = \begin{cases} k(\omega_\mathrm{p}), & \text{for direct pumping} \\ k'(\omega_\mathrm{p}), & \text{for flux-driven TWPAs.}\end{cases} \tag{36}$$

Hence, $\tilde{k}(\omega_\mathrm{p})$ represents the dispersion relation for the nonlinear transmission line in the case of direct pumping and the dispersion relation of the external pump line for flux-driven TWPAs.

Exploiting the space–time translation invariance discussed before, we replace the total amplifier length x with a reference travel time t_r, such that $x = (\Delta z/L_{\mathrm{J},0}C')^{1/2}t_\mathrm{r}$. Hence, we can translate the remaining linear spatial wavevector phase difference to a linear temporal phase mismatch $\Delta\Omega_\mathrm{L}$ by

$$\begin{aligned}\Delta k_{3\mathrm{WM}}x &= \left[\tilde{k}(\omega_\mathrm{p}) - k(\omega) - k(\omega_\mathrm{p} - \omega)\right]x \\ &= \Bigg[\omega_\mathrm{p}\sqrt{\tilde{\Lambda}(\omega_\mathrm{p})} - \omega\sqrt{\Lambda(\omega)} \\ &\quad - (\omega_\mathrm{p} - \omega)\sqrt{\Lambda(\omega_\mathrm{p} - \omega)}\Bigg]t_\mathrm{r} \\ &= \Delta\Omega_\mathrm{L}t_\mathrm{r} \end{aligned} \tag{37}$$

where $\tilde{\Lambda}(\omega_\mathrm{p})$ is equal to $\Lambda(\omega_\mathrm{p})$ from (10) in the case of direct pumping and $\tilde{\Lambda}(\omega_\mathrm{p}) = \Lambda_\mathrm{p}$ from (16) in the case of a flux-driven TWPA.

Note that the mode-dependent propagation time can always be identified with the reference time t_r by $t \to (\Lambda(\omega))^{1/2}t_\mathrm{r}$. Hence, we can derive a propagator $\hat{K}$ that only depends on the total reference propagation time t_r.

A single propagator $\hat{K}$ for the 4WM case is obtained by replacing the continuous pump operators according to (30) and then integrating either (27) or (29) over time. The resulting 4WM propagator $\hat{K}$ also depends on the binary selection parameter m and is given by

$$\begin{aligned}\hat{K} = &\int_0^\infty \Bigg[\frac{\hbar^2 v_\mathrm{ph}(\omega_\mathrm{p})\sqrt{\Delta z C'}\, f^{\Lambda}_{\omega,2\omega_\mathrm{p}-\omega,\omega_\mathrm{p},\omega_\mathrm{p}}}{8\sqrt{2I_\mathrm{c}^3\varphi_0}\, l_\mathrm{q}}\left(\frac{36\varphi_0}{2I_\mathrm{c}c_2\Delta z}\right)^{\frac{m}{2}} \\ &\times \frac{c_4}{c_2^{5/2}}\hat{a}_\mathrm{p}\hat{a}_\mathrm{p}\hat{a}^\dagger_\omega\hat{a}^\dagger_{\omega'}\int_0^x \mathrm{e}^{\mathrm{i}\Delta k_\mathrm{L}z}\mathrm{d}z + \mathrm{H.c.}\Bigg] \\ &\times\left[\kappa^2\left(L'_\mathrm{p}C'_\mathrm{p}\right)^{\frac{1}{2}}\right]^{1-m}\mathrm{d}\omega \\ &+ \int_0^\infty \frac{\hbar^2 v_\mathrm{ph}(\omega_\mathrm{p})\sqrt{\Delta z C'}\, f^{\Lambda}_{\omega,\omega,\omega_\mathrm{p},\omega_\mathrm{p}}}{4\sqrt{2I_\mathrm{c}^3\varphi_0}\, l_\mathrm{q}}\left(\frac{36\varphi_0}{2I_\mathrm{c}c_2\Delta z}\right)^{\frac{m}{2}} \\ &\times \frac{c_4}{c_2^{5/2}}\hat{a}^\dagger_\mathrm{p}\hat{a}_\mathrm{p}\hat{a}^\dagger_\omega\hat{a}_\omega\int_0^x \mathrm{e}^{\mathrm{i}\Delta k_\mathrm{XPM}z}\mathrm{d}z \\ &\times\left[\kappa^2\left(L'_\mathrm{p}C'_\mathrm{p}\right)^{\frac{1}{2}}\right]^{1-m}\mathrm{d}\omega \\ &+ \frac{\hbar^2 v_\mathrm{ph}(\omega_\mathrm{p})\sqrt{\Delta z C'}\, f^{\Lambda}_{\omega_\mathrm{p},\omega_\mathrm{p},\omega_\mathrm{p},\omega_\mathrm{p}}}{16\sqrt{2I_\mathrm{c}^3\varphi_0}\, l_\mathrm{q}}\left(\frac{36\varphi_0}{2I_\mathrm{c}c_2\Delta z}\right)^{\frac{1}{2}} \\ &\times \frac{c_4}{c_2^{5/2}}\hat{a}^\dagger_\mathrm{p}\hat{a}_\mathrm{p}\hat{a}^\dagger_\mathrm{p}\hat{a}_\mathrm{p}\int_0^x \mathrm{e}^{\mathrm{i}\Delta k_\mathrm{SPM}z}\mathrm{d}z\,(2^m - 1) \\ &+ \int_{-\infty}^{\infty}\int_0^\infty \sum_n \hbar\omega_n\hat{b}^\dagger_n(\omega)\hat{b}_n(\omega)\mathrm{d}\omega\mathrm{d}t \\ &+ \int_{-\infty}^{\infty}\int_0^\infty \sum_n \hbar\left[g_n(\omega)\hat{b}^\dagger_n(\omega)\hat{a}_\omega\mathrm{e}^{-i\omega t} + \mathrm{H.c.}\right]\mathrm{d}\omega\mathrm{d}t\,. \end{aligned} \tag{38}$$

Here, $\Delta k_\mathrm{XPM} = 0$, $\Delta k_\mathrm{SPM} = 0$, and the remaining wavevector phase difference $\Delta k_{4\mathrm{WM}}$ in (38) is given by

$$\Delta k_{4\mathrm{WM}} = 2\tilde{k}(\omega_\mathrm{p}) - k(\omega) - k(2\omega_\mathrm{p} - \omega)\,. \tag{39}$$

We can again exploit the space–time translation symmetry and replace the total length of the amplifier x by $(\Delta z/L_{\mathrm{J},0}C')^{1/2}t_\mathrm{r}$. Hence, the temporal linear phase mismatch $\Delta\Omega_\mathrm{L}$ in the 4WM case is given by

$$\begin{aligned}\Delta k_{4\mathrm{WM}}x &= \left[2\tilde{k}(\omega_\mathrm{p}) - k(\omega) - k(2\omega_\mathrm{p} - \omega)\right]x \\ &= \Bigg[2\omega_\mathrm{p}\sqrt{\tilde{\Lambda}(\omega_\mathrm{p})} - \omega\sqrt{\Lambda(\omega)} \\ &\quad -(2\omega_\mathrm{p} - \omega)\sqrt{\Lambda(2\omega_\mathrm{p} - \omega)}\Bigg]t_\mathrm{r} = \Delta\Omega_\mathrm{L}t_\mathrm{r}\,. \end{aligned} \tag{40}$$

The equation of motion for the mode annihilation operator $\hat{a}_\omega$, with respect to the reference propagation time t_r, can now be calculated from

$$\frac{\partial\hat{a}_\omega}{\partial t_\mathrm{r}} = \frac{\mathrm{i}}{\hbar}\left[\frac{\mathrm{d}\hat{K}}{\mathrm{d}t_\mathrm{r}}, \hat{a}_\omega\right] \tag{41}$$

similar to [22]. According to [22], [50], and [52], we can obtain analytic solutions by assuming a strong, monochromatic, undepleted, classical pump, which is described by a classical amplitude instead of an operator. With the term undepleted, we mean that the interaction between the individual modes does not affect the strong classical amplitude. As already stated in [22], this is a bold assumption since it violates energy conservation. As a consequence of this approximation, the energy added to the signal and idler modes comes out of nowhere. However, this approximation seems justified for the case of a relatively small total amplifier length such that the cumulative signal and idler energies are still orders of magnitude smaller than the pump tone. The approximation is given by [22]

$$\sqrt{\frac{\hbar}{2C'\omega_\mathrm{p}l_\mathrm{q}}}\hat{a}_\mathrm{p} \to -\frac{\mathrm{i}}{2}A_\mathrm{p} \tag{42}$$

where A_p is a classical mode amplitude. Since the pump is not depleted while traveling through the amplifier, it is only affected by SPM for internal pumping and travels completely unperturbed in the external flux line. This decouples the equation of motion from the remaining system, which means it can be easily solved analytically. Hence, the pump amplitude is given by

$$A_\mathrm{p} = A_{\mathrm{p},0}\,\mathrm{e}^{\mathrm{i}\theta_\mathrm{p}\sqrt{\Lambda(\omega_\mathrm{p})}t_\mathrm{r}} \tag{43}$$

with

$$\theta_\mathrm{p} = -\frac{I_\mathrm{p}^2\sqrt{\Delta z}\, f^{\Lambda}_{\omega_\mathrm{p},\omega_\mathrm{p},\omega_\mathrm{p},\omega_\mathrm{p}}}{16\omega_\mathrm{p}\sqrt{2I_\mathrm{c}^3\varphi_0}}\cdot\frac{c_4}{c_2^{5/2}}\left(\frac{36\varphi_0}{2I_\mathrm{c}c_2\Delta z}\right)^{\frac{1}{2}}. \tag{44}$$

Here, I_p is the initial pump current at the input of the amplifier, and $A_{\mathrm{p},0}$ is the initial pump amplitude. Both are related through the characteristic impedance of the transmission line the pump wave is propagating in. Thus, $\theta_\mathrm{p}(\omega) = 0$ for flux-driven TWPAs, since there is no SPM, and it holds that $A_\mathrm{p} = A_{\mathrm{p},0}$.

The equations of motion for the remaining signal and idler annihilation and creation operators, $\hat{a}_\omega$ and $\hat{a}^\dagger_{\omega'}$, can be found by evaluating (41) with the respective propagators from (32) or (38), with the corresponding linear phase mismatch from (37) or (40), respectively. In the resulting set

of equations, we can summarize the effect of XPM in terms of a frequency-dependent coefficient $\theta(\omega)$, given by

$$\theta(\omega) = -\frac{I_\mathrm{p}^2\omega\Lambda(\omega)\Lambda^2(\omega_\mathrm{p})\sqrt{\Delta z}}{8\sqrt{2I_\mathrm{c}^3\varphi_0}}\cdot\frac{c_4}{c_2^{5/2}}\left(\frac{36\varphi_0}{2I_\mathrm{c}c_2\Delta z}\right)^{\frac{m}{2}} \times\left[\kappa^2\left(L_\mathrm{p}'C_\mathrm{p}'\right)^{\frac{1}{2}}\right]^{1-m}\left[\frac{\varphi_0 C_\mathrm{p}'}{2I_\mathrm{c}c_2\Delta z L_\mathrm{p}'}\right]^{\frac{m-1}{2}}. \quad (45)$$

Hence, we find the total phase mismatch $\Delta\Omega$, which is jointly due to chromatic dispersion, as well as self- and XPM, to be equal to

$$\Delta\Omega = \Delta\Omega_\mathrm{L} - \theta(\omega)\sqrt{\Lambda(\omega)} - \theta(\omega_\mathrm{p}-\omega)\sqrt{\Lambda(\omega_\mathrm{p}-\omega)} + \theta_\mathrm{p}\sqrt{\Lambda(\omega_\mathrm{p})} \quad (46)$$

in the 3WM operation regime, and

$$\Delta\Omega = \Delta\Omega_\mathrm{L} - \theta(\omega)\sqrt{\Lambda(\omega)} - \theta(2\omega_\mathrm{p}-\omega)\sqrt{\Lambda(2\omega_\mathrm{p}-\omega)} + 2\theta_\mathrm{p}\sqrt{\Lambda(\omega_\mathrm{p})} \quad (47)$$

for 4WM. Note that $\theta_\mathrm{p} = 0$ for flux-driven TWPAs.

Using the total phase-mismatch $\Delta\Omega$, we introduce another co-rotating frame similar to [22], given by

$$\hat{A}_\omega = \hat{a}_\omega \exp\left\{-\mathrm{i}\left[\theta(\omega)\sqrt{\Lambda(\omega)} + \frac{\Delta\Omega}{2}\right]t_\mathrm{r}\right\}. \quad (48)$$

Within this co-rotating frame, the system of coupled first-order equations of motion for the signal mode annihilation operator and the idler mode creation operator assumes the following simple form:

$$\begin{bmatrix}\frac{\partial\hat{A}_\omega}{\partial t_\mathrm{r}}\\ \frac{\partial\hat{A}^\dagger_{\omega'}}{\partial t_\mathrm{r}}\end{bmatrix} = \begin{bmatrix}-\frac{\gamma(\omega)}{2} - \frac{\mathrm{i}\Delta\Omega}{2} & \chi'\left[\Lambda(\omega)\Lambda(\omega')\right]^{\frac{1}{4}}\\ \chi'^{*}\left[\Lambda(\omega)\Lambda(\omega')\right]^{\frac{1}{4}} & -\frac{\gamma(\omega')}{2} + \frac{\mathrm{i}\Delta\Omega}{2}\end{bmatrix}\begin{bmatrix}\hat{A}_\omega\\ \hat{A}^\dagger_{\omega'}\end{bmatrix} + \begin{bmatrix}\hat{f}(\omega)\\ \hat{f}^\dagger(\omega')\end{bmatrix} \quad (49)$$

with $\omega' = \omega_\mathrm{p} - \omega$ for 3WM and $\omega' = 2\omega_\mathrm{p} - \omega$ for 4WM.

The coefficient χ' is either the 3WM or 4WM interaction strength. This coefficient is ultimately responsible for the parametric gain of the TWPA. For 3WM, it can be evaluated to

$$\chi' = \frac{I_\mathrm{p}\Lambda(\omega_\mathrm{p})\sqrt{\omega(\omega_\mathrm{p}-\omega)\Lambda(\omega)\Lambda(\omega_\mathrm{p}-\omega)}}{8I_\mathrm{c}}\frac{c_3}{c_2^2} \times 3^m\left(\frac{\varphi_0}{2I_\mathrm{c}c_2\Delta z}\right)^{\frac{m-1}{2}}\left[\kappa\left(L_\mathrm{p}'C_\mathrm{p}'\right)^{\frac{1}{4}}\right]^{1-m}\left[\frac{C_\mathrm{p}'}{L_\mathrm{p}'}\right]^{\frac{m-1}{4}} \quad (50)$$

with the binary selection parameter $m \in \{0, 1\}$. For 4WM, the interaction strength is given by

$$\chi' = \frac{\mathrm{i}I_\mathrm{p}^2\Lambda^2(\omega_\mathrm{p})\sqrt{\Delta z\omega(2\omega_\mathrm{p}-\omega)\Lambda(\omega)\Lambda(2\omega_\mathrm{p}-\omega)}}{16\sqrt{2I_\mathrm{c}^3\varphi_0}}\frac{c_4}{c_2^{5/2}} \times\left(\frac{36\varphi_0}{2I_\mathrm{c}c_2\Delta z}\right)^{\frac{m}{2}}\left[\kappa^2\left(L_\mathrm{p}'C_\mathrm{p}'\right)^{\frac{1}{2}}\right]^{1-m}\left[\frac{\varphi_0 C_\mathrm{p}'}{2I_\mathrm{c}c_2\Delta z L_\mathrm{p}'}\right]^{\frac{m-1}{2}}. \quad (51)$$

The damping factors $\gamma(\omega)$ and the noise operators $\hat{f}(\omega)$ are similar to [17] and [22]. They arise from the formal integration of the equation of motion of the bath operators $\hat{b}_n$, assuming a memoryless Markovian system with closely spaced bath modes over a continuous frequency spectrum [47] and [57]. It shall be noted here that distributed losses in quantum models for TWPAs have also been introduced by means of a continuous input-output theory in [58] and [59]. The damping rates $\gamma(\omega)$ are given by

$$\gamma(\omega) = 2\pi\mathcal{D}(\omega)g(\omega)^2\sqrt{\Lambda(\omega)} \quad (52)$$

where $\mathcal{D}(\omega)$ is the 1-D density of states and $g(\omega)$ is the continuous frequency version of the bath coupling constants g_n from (25). The fluctuation operators $\hat{f}(\omega)$ from (49) are given by

$$\hat{f}(\omega) = -\mathrm{i}\sum_n g_n(\omega)\sqrt{\Lambda(\omega)}\hat{b}_{n,0}(\omega) \times \mathrm{e}^{-\mathrm{i}\left[(\omega_n-\omega)\sqrt{\Lambda(\omega_n)}+\theta(\omega)\sqrt{\Lambda(\omega)}+\Delta\Omega/2\right]t_\mathrm{r}} \quad (53)$$

with the operator $\hat{b}_{n,0}$ describing the initial bath occupation. The phenomenological loss rates from (52) can be associated with the loss tangent [36] of the substrate material according to [22] and [35]

$$\gamma(\omega) \mapsto \omega\sqrt{\Lambda(\omega)}\tan\delta\,. \quad (54)$$

Overall, (49) represents the Heisenberg equation of motion for any nonlinear superconducting transmission line with Josephson nonlinear elements, accounting for nonlinearities up to third order. The generic Josephson nonlinear element is represented through the coefficients c_2, c_3, and c_4. Our black-box quantum simulation framework for superconducting TWPAs is sketched in Fig. 3. Equation (49), i.e., the Heisenberg equations of motion are the core of the framework, which are independent of the actual realization of the nonlinear elements. The coefficients c_2, c_3, and c_4 are obtained independently of the system dynamics using a Taylor expansion of the nonlinear current–phase relation according to either (3) or (5). The nonlinear parameters are fed from the green device description block in Fig. 3 into the blue block, representing (49). Additionally, the parameters describing the scenario (orange block) are also supplied to the system. This device-independent nonlinear black-box quantum model is the core achievement of this article.

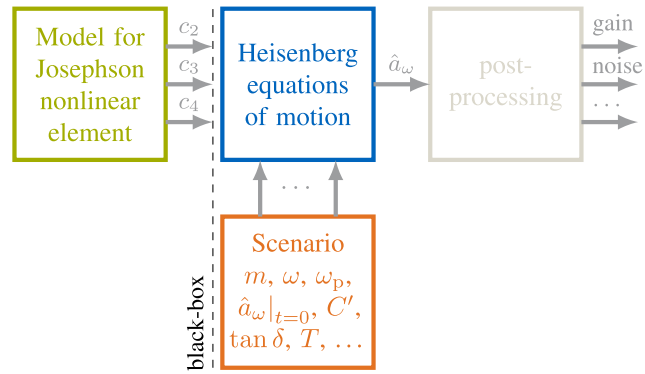

Fig. 3. Functional blocks of the black-box quantum model for superconducting TWPAs.

Since the calculation of the system dynamics is completely decoupled from the physical realization of the Josephson

nonlinear elements, the presented model can prove useful in designing and optimizing different TWPA architectures with respect to gain, added noise, and quantum effects.

V. Results

Analytic solutions to the Heisenberg equations of motion have been found in [22] for the 4WM case, using a single Josephson junction for the nonlinear element. Important quantities, such as, e.g., the gain and the equivalent added quantum noise of the amplifier, can then be obtained from the analytic solution of the signal annihilation operator in a post-processing step (see Fig. 3). To calculate the gain and added noise of a TWPA with a black-box nonlinear element, we are interested in the number of energy quanta in the signal mode within a narrow signal bandwidth B_s. The signal photon number after a reference propagation time of t_r at the output of the amplifier is then given by

$$N_\mathrm{s} = \int_{\omega-\frac{B_\mathrm{s}}{2}}^{\omega+\frac{B_\mathrm{s}}{2}} \langle \hat{A}_\omega^\dagger \hat{A}_{\tilde{\omega}} \rangle \mathrm{d}\tilde{\omega}\,. \tag{55}$$

Inserting the analytic solution from [22] yields

$$\begin{aligned} N_\mathrm{s} = {} & \bar{n}(\omega) + \big[N_{\mathrm{s},0} - \bar{n}(\omega)\big]\zeta_1(\omega,t_\mathrm{r})\zeta_1^*(\omega,t_\mathrm{r})\mathrm{e}^{-\frac{\gamma(\omega)+\gamma(\omega')}{2}t_\mathrm{r}} \\ & + C_{\mathrm{si},0}\zeta_1(\omega,t_\mathrm{r})\zeta_2^*(\omega,t_\mathrm{r})\mathrm{e}^{-\frac{\gamma(\omega)+\gamma(\omega')}{2}t_\mathrm{r}} \\ & + \big[N_{\mathrm{i},0} + \bar{n}(\omega) + 1\big]\zeta_2(\omega,t_\mathrm{r})\zeta_2^*(\omega,t_\mathrm{r})\mathrm{e}^{-\frac{\gamma(\omega)+\gamma(\omega')}{2}t_\mathrm{r}} \\ & + C_{\mathrm{si},0}^*\zeta_2(\omega,t_\mathrm{r})\zeta_1^*(\omega,t_\mathrm{r})\mathrm{e}^{-\frac{\gamma(\omega)+\gamma(\omega')}{2}t_\mathrm{r}} \\ & + \big[\bar{n}(\omega) + \bar{n}(\omega') + 1\big]\frac{\bar{F}(\omega,t_\mathrm{r})}{\bar{R}(\omega)}\mathrm{e}^{-\frac{\gamma(\omega)+\gamma(\omega')}{2}t_\mathrm{r}} \end{aligned} \tag{56}$$

where $N_{\mathrm{s},0}$ is the initial signal photon number in the weak photon field at the input of the amplifier, $N_{\mathrm{i},0}$ is the initial idler photon number at frequency ω', and $C_{\mathrm{si},0}$ is the initial signal-idler correlation. Similar to [22], we assume that the bath is thermally populated with an average occupation of $\bar{n}(\omega)$ at frequency ω according to Bose–Einstein statistics. The independent part $\bar{F}(\omega,t_\mathrm{r})$ evolves according to

$$\begin{aligned} & \bar{F}(\omega,t) \\ & = -|g|^2|\rho|^2\gamma(\omega')^2\zeta_1(\omega,t)\zeta_1^*(\omega,t) \\ & \quad + |g|^2|\rho|^2\big[\gamma(\omega)\gamma(\omega') + \gamma(\omega')^2\big]\big[\zeta_2(\omega,t)\zeta_2^*(\omega,t)\big] \\ & \quad - \gamma(\omega)\gamma(\omega')\big|g\rho\zeta_1(\omega,t) + \big[2g\eta + \gamma(\omega')\big]\zeta_2(\omega,t)\big|^2 \\ & \quad + |g|^2|\rho|^2\big[\gamma(\omega)\gamma(\omega') + \gamma(\omega')^2\big]\mathrm{e}^{\frac{\gamma(\omega)+\gamma(\omega')}{2}t} \end{aligned} \tag{57}$$

with the time-independent denominator $\bar{R}(\omega)$, given by

$$\begin{aligned} \bar{R}(\omega) = {} & \gamma(\omega)\gamma(\omega')\big[4|g|^2|\eta|^2 + \gamma(\omega)\gamma(\omega')\big] \\ & - |g|^2|\rho|^2\big[\gamma(\omega) + \gamma(\omega')\big]^2\,. \end{aligned} \tag{58}$$

The time-evolution of N_s is governed by the functions $\zeta_1(\omega,t_\mathrm{r})$ and $\zeta_2(\omega,t_\mathrm{r})$, which are the inherent solutions to (49). They are given by

$$\zeta_1(\omega,t) = \cosh(gt) - \eta(\omega)\sinh(gt) \tag{59}$$

$$\zeta_2(\omega,t) = \rho(\omega)\sinh(gt) \tag{60}$$

TABLE I
Parameters for a Flux-Driven SNAIL-Based TWPA

Parameter	Symbol	Value
Critical current	I_c	3.85 µA
Asymmetry ratio	α	0.12
Bias phase difference	φ_B	$2\pi \cdot 0.3577$
Unit cell ground capacitance	C	115 fF
Unit cell number	N_cell	400
Unit cell physical length	Δz	15 µm
Effective dispersion capacitance	$C_\mathrm{disp}^\mathrm{eff}$	50 fF
Pump coupling coefficients	κ	0.012
Pump frequency	$\omega_\mathrm{p}/2\pi$	12 GHz
Pump power	P_p	−53 dBm
Substrate loss tangent	$\tan\delta$	0.0025
Flux-line capacitance	$C_\mathrm{p}'\Delta z$	115 fF
Flux-line inductance	$L_\mathrm{p}'\Delta z$	287.5 nH

with the frequency-dependent coefficients

$$\eta(\omega) = \frac{\gamma(\omega) - \gamma(\omega') + 2\mathrm{i}\Delta\Omega}{4g} \tag{61}$$

$$\rho(\omega) = -\frac{\chi'\big[\Lambda(\omega)\Lambda(\omega')\big]^{\frac{1}{4}}}{g}\,. \tag{62}$$

The exponential gain rate g in (59)–(62), is determined as

$$g = \sqrt{\left(\frac{\gamma(\omega) - \gamma(\omega') + 2\mathrm{i}\Delta\Omega}{4}\right)^2 + |\chi'|^2\sqrt{\Lambda(\omega)\Lambda(\omega')}}\,. \tag{63}$$

Equation (56) describes the temporal evolution of the average energy dynamics in the TWPA. It can be decomposed into parametric gain and noise that is added by the amplifier.

A. Parametric Gain

We can identify an expression for the parametric gain of a TWPA from the term in (56), which is multiplied with the initial signal photon number $N_{\mathrm{s},0}$ at the input of the amplifier. Thus, an analytic expression for the gain G of the TWPA, after a reference propagation time t_r at the amplifier output, is given by

$$G = \zeta_1(\omega,t_\mathrm{r})\zeta_1^*(\omega,t_\mathrm{r})\mathrm{e}^{-\frac{\gamma(\omega)+\gamma(\omega')}{2}t_\mathrm{r}}\,. \tag{64}$$

The gain depends on the black-box nonlinear coefficients c_2, c_3, and c_4 and can be calculated by (64) independently for 3WM and 4WM operation, as well as for direct pumping and flux-driven TWPAs. For example, we evaluate the parametric gain for two devices with different operation modes and pumping schemes, both using (64). The first device is a single junction TWPA from [22] and [60], where experimental data for the gain and added noise is readily available. As a second device, we propose a flux-driven SNAIL-based TWPA with the parameters in Table I. Note that in both cases, no hidden fitting parameters are used besides the values given in [22] and [60] and Table I, respectively.

The gain spectrum of the first device with directly driven single Josephson junctions is given by the dashed orange line in Fig. 4(a). The maximum gain of around 10 dB is

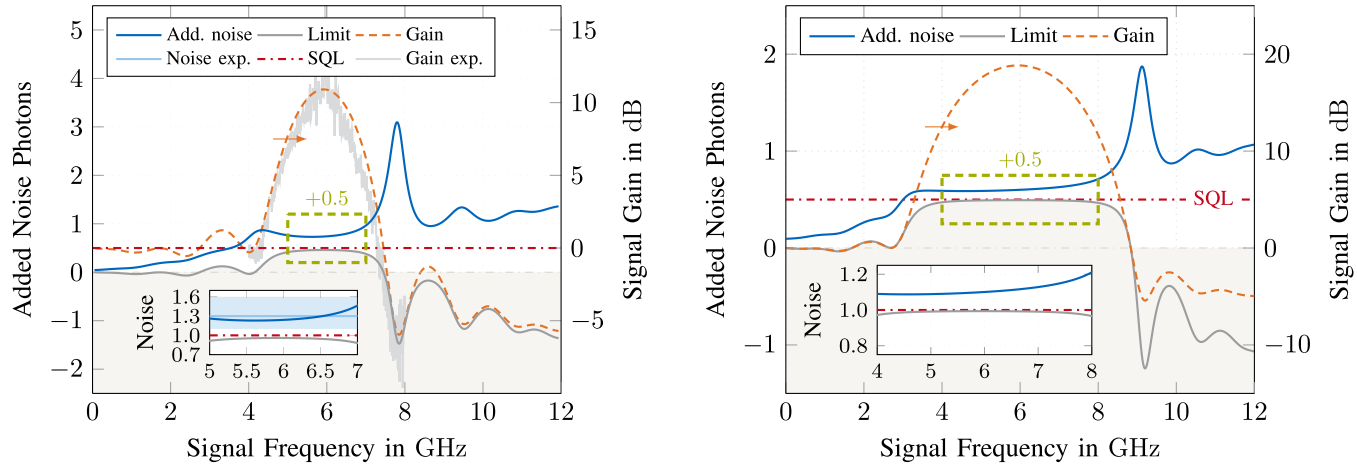

Fig. 4. Gain and added noise of two different devices. (a) Directly pumped TWPA featuring a single Josephson junction as a nonlinear element. (b) Flux-driven SNAIL-based TWPA with parameters as given in Table I. The solid blue curves depict the added noise of the amplifiers. The dashed orange lines represent the gain. The minimum added noise is plotted by the dark gray lines, where the ivory-shaded backgrounds mark the forbidden areas for the added noise. The insets show a zoom-in of the total input noise in the useable frequency ranges between 5 and 7 and 4 and 8 GHz, respectively.

around 6 GHz. Note, however, that due to the 4WM operation, the signal frequency must be sufficiently far apart from the pump tone at 5.97 GHz to be able to separate the signal and pump modes at the output of the amplifier. The measured gain spectrum from [60] is plotted in light-gray color in the background for comparison. The experimental results closely follow the predicted gain from (64), which was obtained with the parameters given in [22] and [60], without any additional data fitting. The dashed orange curve in Fig. 4(b) shows the gain of the proposed flux-driven SNAIL-based TWPA obtained by evaluating (64) with the parameters in Table I. Compared to the directly pumped single junction TWPA, the gain in dB is almost twice as large. The SNAIL-based TWPA also has a substantially increased bandwidth.

B. Added Noise

The added noise in the system is given by the remaining terms in (56), which cannot be attributed to the parametric gain. The added noise is then calculated based on the linear amplifier model introduced in [12] and [22]. There, the noise at the output of a linear amplifier, i.e., $N_\mathrm{s} = G \cdot N_{\mathrm{s},0}$, can be decomposed into contributions of the amplified input fluctuations and the noise added by the internal degrees of freedom of the amplifier. The added noise of the amplifier is then quantified as the equivalent number of energy quanta added to the input of the amplifier if an ideal noiseless amplifier with gain G would be used instead [12]. This approach has been routinely applied to study added quantum noise in TWPAs [58], [61], [62]. The symmetric variance

$$|\Delta\hat{A}_{\omega,t_\mathrm{r}}|^2 = \int_{\omega-\frac{B_\mathrm{s}}{2}}^{\omega+\frac{B_\mathrm{s}}{2}} \left\langle \hat{A}_{\omega,t_\mathrm{r}}\hat{A}^\dagger_{\tilde{\omega},t_\mathrm{r}} + \hat{A}^\dagger_{\omega,t_\mathrm{r}}\hat{A}_{\tilde{\omega},t_\mathrm{r}} \right\rangle \mathrm{d}\tilde{\omega} = N_\mathrm{s} + \frac{1}{2} \tag{65}$$

provides a measure for the mean-square fluctuations $|\Delta\hat{A}_{\omega,t_\mathrm{r}}|^2$ of the weak photon field within the narrow signal bandwidth B_s. The simple linear amplifier model from [12] then predicts the output fluctuations $|\Delta\hat{A}_{\omega,t_\mathrm{r}}|^2$ to be the sum of the amplified input fluctuations $|\Delta\hat{A}_{\omega,0}|^2$ and the noise $|\Delta\hat{\mathcal{F}}|^2_\mathrm{op}$ due to the amplifier's internal degrees of freedom. The equivalent number of added input photons A is thus given by the intrinsic fluctuations $|\Delta\hat{\mathcal{F}}|^2_\mathrm{op}$ divided by the parametric gain G of the amplifier. Finally, we can express the added noise of any TWPA with a nonlinearity up to third order, including noise due to substrate losses by

$$A = \frac{|\Delta\hat{A}_{\omega,t_\mathrm{r}}|^2}{G} - |\Delta\hat{A}_{\omega,0}|^2 = \frac{2N_\mathrm{s}+1}{2G} - N_{\mathrm{s},0} - \frac{1}{2}. \tag{66}$$

Inserting (56) and (64) into (66) yields

$$\begin{aligned} A = {} & \left[\bar{n}(\omega) + \frac{1}{2}\right]\left[\frac{1}{\zeta_1(\omega,t_\mathrm{r})\zeta_1^*(\omega,t_\mathrm{r})\mathrm{e}^{-\frac{\gamma(\omega)+\gamma(\omega')}{2}t_\mathrm{r}}} - 1\right] \\ & + C_{\mathrm{si},0}\frac{\zeta_2^*(\omega,t_\mathrm{r})}{\zeta_1^*(\omega,t_\mathrm{r})} + C_{\mathrm{si},0}^*\frac{\zeta_2(\omega,t_\mathrm{r})}{\zeta_1(\omega,t_\mathrm{r})} \\ & + \left[N_{\mathrm{i},0} + \bar{n}(\omega) + 1\right]\frac{\zeta_2(\omega,t_\mathrm{r})\zeta_2^*(\omega,t_\mathrm{r})}{\zeta_1(\omega,t_\mathrm{r})\zeta_1^*(\omega,t_\mathrm{r})} \\ & + \left[\bar{n}(\omega) + \bar{n}(\omega') + 1\right]\frac{\bar{F}(\omega,t_\mathrm{r})}{\bar{R}(\omega)\zeta_1(\omega,t_\mathrm{r})\zeta_1^*(\omega,t_\mathrm{r})}. \end{aligned} \tag{67}$$

The lower bound for the added input noise A for phase-insensitive linear amplifiers with a gain larger than or equal to unity

$$A \geq \frac{1}{2}\left|1 - \frac{1}{G}\right|, \quad \text{for } G \geq 1 \tag{68}$$

was derived in [12]. In the limit of $G \to \infty$, (68) reduces to the well-known half-photon standard quantum limit (SQL).

Similar to the treatment of the amplifier gain in Section V-A, we want to demonstrate the calculation of the added noise for the two exemplary TWPAs introduced above. Fig. 4(a) shows the added noise of the directly pumped single-junction TWPA from [22] and [60] (blue curve). The dark-gray curve and the shaded background area represent the lower bound on the added noise according to (68). The inset

of Fig. 4(a) shows a zoom-in into the usable frequency range marked by the dashed green box. The inset shows the total input noise, also accounting for the half-photon uncertainty of the input signal mode. It can be seen that the device operates close to the SQL at around 1.3 equivalent total input noise photons, which is in excellent agreement with experimental observations [60], also without any additional fitting parameters. The added noise according to (67) for the flux-driven SNAIL-based TWPA with the values proposed in Table I is given in Fig. 4(b), together with the lower bound in (68). The inset shows that the proposed SNAIL-based TWPA also outperforms the single-junction TWPA in terms of total equivalent input noise, which is evaluated to around 1.1 photons in theory. We are looking forward to experimental confirmation of the predicted gain and added noise of our proposed design.

C. Optimization of Nonlinear Parameters

Since the proposed black-box quantum model in (49) is completely independent of the physical realization of the Josephson nonlinear elements, it is perfectly suitable for the parameter optimization of given nonlinear junction topologies. Coupled with a powerful system identification toolbox, the model could also be used to propose new, more efficient, higher gain, larger bandwidth, and lower noise designs. We want to discuss how to obtain optimized parameters for three different types of nonlinear junction topologies. For this, we discuss RF-SQUIDs, dc-SQUIDs, and SNAILs to identify their optimum operation regimes. The respective junction topologies can be found in Fig. 2(b)–(d). We refrain from discussing single Josephson junction nonlinearities since they do not possess any degree of freedom besides choosing a critical current. Similarly, we do not discuss the recently proposed gradiometric SNAIL [28] here, as it possesses an additional degree of freedom for the independent upper and lower loops.

The loop-like geometries of the RF-SQUID, the dc-SQUID, and the SNAIL allow for an additional constant flux threading, introducing a constant bias phase φ_{B}, as discussed in Section III. Something similar could also be achieved by impressing a constant current i_0, using a bias-tee, as mentioned before [38]. We now use this constant flux threading as a degree of freedom for choosing an optimal parameter set c_2, c_3, and c_4 for the nonlinear elements. Note that a SNAIL has an additional degree of freedom, given by the asymmetry ratio α. In principle, the RF-SQUID also has an extra degree of freedom, provided by the geometric inductance L_{g}. However, it is hard to tune the geometric inductance while keeping the impedance of the transmission line [36]. Also, L_{g} only influences the screening parameter β_{L} of the RF-SQUID, which is typically neglected for dc-SQUIDs and SNAILs, as the Josephson inductance is usually much larger than the geometric inductance.

1) RF-SQUID: The current-phase relation of the RF-SQUID is given by [26]

$$i(\varphi) = \frac{I_{\mathrm{c}}}{\beta_{\mathrm{L}}}\varphi + I_{\mathrm{c}}\left[\sin\left(\varphi_{\mathrm{J},0} + \varphi\right) - \sin\left(\varphi_{\mathrm{J},0}\right)\right] \tag{69}$$

with the screening parameter $\beta_{\mathrm{L}} = L_{\mathrm{g}} I_{\mathrm{c}}/\varphi_0$ and the induced phase $\varphi_{\mathrm{J},0}$, given by the implicit equation

$$\varphi_{\mathrm{J},0} + \beta_{\mathrm{L}} \sin\left(\varphi_{\mathrm{J},0}\right) = \varphi_{\mathrm{ext}} \tag{70}$$

where φ_{ext} is the total external flux threading, according to Section III. The minimum potential energy is attained for $i(\varphi^*) = 0$, and thus $\varphi^* = 0$. Hence, according to equations (6)-(8), the coefficients c_2, c_3, and c_4 are expressed by

$$c_2 = \frac{1}{2}\left[\frac{1}{\beta_{\mathrm{L}}} + \cos\left(\varphi_{\mathrm{J},0}(\varphi_{\mathrm{B}})\right)\right] \tag{71}$$

$$c_3 = \begin{cases} -\dfrac{\sin\left(\varphi_{\mathrm{J},0}(\varphi_{\mathrm{B}})\right)}{6}, & \text{for } m = 1 \\ \dfrac{1}{2}\dfrac{\mathrm{d}}{\mathrm{d}\varphi_{\mathrm{ext}}}\cos\left(\varphi_{\mathrm{J},0}(\varphi_{\mathrm{ext}})\right)\Big|_{\varphi_{\mathrm{ext}}=\varphi_{\mathrm{B}}}, & \text{for } m = 0 \end{cases} \tag{72}$$

$$c_4 = \begin{cases} -\dfrac{\cos\left(\varphi_{\mathrm{J},0}(\varphi_{\mathrm{B}})\right)}{24}, & \text{for } m = 1 \\ \dfrac{1}{4}\dfrac{\mathrm{d}^2}{\mathrm{d}\varphi_{\mathrm{ext}}^2}\cos\left(\varphi_{\mathrm{J},0}(\varphi_{\mathrm{ext}})\right)\Big|_{\varphi_{\mathrm{ext}}=\varphi_{\mathrm{B}}}, & \text{for } m = 0 \end{cases} \tag{73}$$

given a solution for $\varphi_{\mathrm{J},0}$ from the implicit equation in (70) [42]. As always, $m = 1$ refers to the case of direct pumping, whereas $m = 0$ implies flux drive.

2) dc-SQUID: The current–phase relation of the dc-SQUID, on the other hand, is given by [27]

$$i(\varphi) = 2I_{\mathrm{c}}\left|\cos\left(\frac{\varphi_{\mathrm{ext}}}{2}\right)\right|\sin(\varphi) \tag{74}$$

with two identical junctions with critical current I_{c}. Also, here, it trivially holds that $\varphi^* = 0$. The coefficients for the dc-SQUID are then given by

$$c_2 = \left|\cos\left(\frac{\varphi_{\mathrm{B}}}{2}\right)\right| \tag{75}$$

$$c_3 = \begin{cases} 0, & \text{for } m = 1 \\ -\dfrac{\sin(\varphi_{\mathrm{B}})}{4\left|\cos\left(\frac{\varphi_{\mathrm{B}}}{2}\right)\right|}, & \text{for } m = 0 \end{cases} \tag{76}$$

$$c_4 = \begin{cases} -\dfrac{\left|\cos\left(\frac{\varphi_{\mathrm{B}}}{2}\right)\right|}{12}, & \text{for } m = 1 \\ -\dfrac{\cos^2(\varphi_{\mathrm{B}})}{8\left|\cos\left(\frac{\varphi_{\mathrm{B}}}{2}\right)\right|}, & \text{for } m = 0 \end{cases} \tag{77}$$

where we have neglected the geometric inductance in favor of the large inductance of the Josephson junctions [42].

3) SNAIL: The current–phase relation of a SNAIL with asymmetry ratio $\alpha \in [0, 1]$ is given by [31] and [39]

$$i(\varphi) = \alpha I_{\mathrm{c}} \sin(\varphi) + I_{\mathrm{c}} \sin\left(\frac{\varphi - \varphi_{\mathrm{ext}}}{n}\right) \tag{78}$$

where n denotes the number of large junctions. Here, the calculation of the minimum potential energy flux φ^* from $i(\varphi^*) = 0$ is a more intricate procedure [42]. It holds that

$$i(\varphi^*) = \alpha I_{\mathrm{c}} \sin\left(\varphi^*\right) + I_{\mathrm{c}} \sin\left(\frac{\varphi^* - \varphi_{\mathrm{ext}}}{n}\right) = 0 \tag{79}$$

where an analytic solution for φ^* is not readily apparent. Hence, by introducing a complex variable $z = \exp\left(\mathrm{i}\varphi^*/n\right)$, we can equivalently solve for the zeros of the polynomial

$$z^{2n} + \frac{1}{\alpha}\mathrm{e}^{-\mathrm{i}\frac{\varphi_{\mathrm{ext}}}{n}} z^{n+1} - \frac{1}{\alpha}\mathrm{e}^{\mathrm{i}\frac{\varphi_{\mathrm{ext}}}{n}} z^{n-1} - 1 = 0 \tag{80}$$

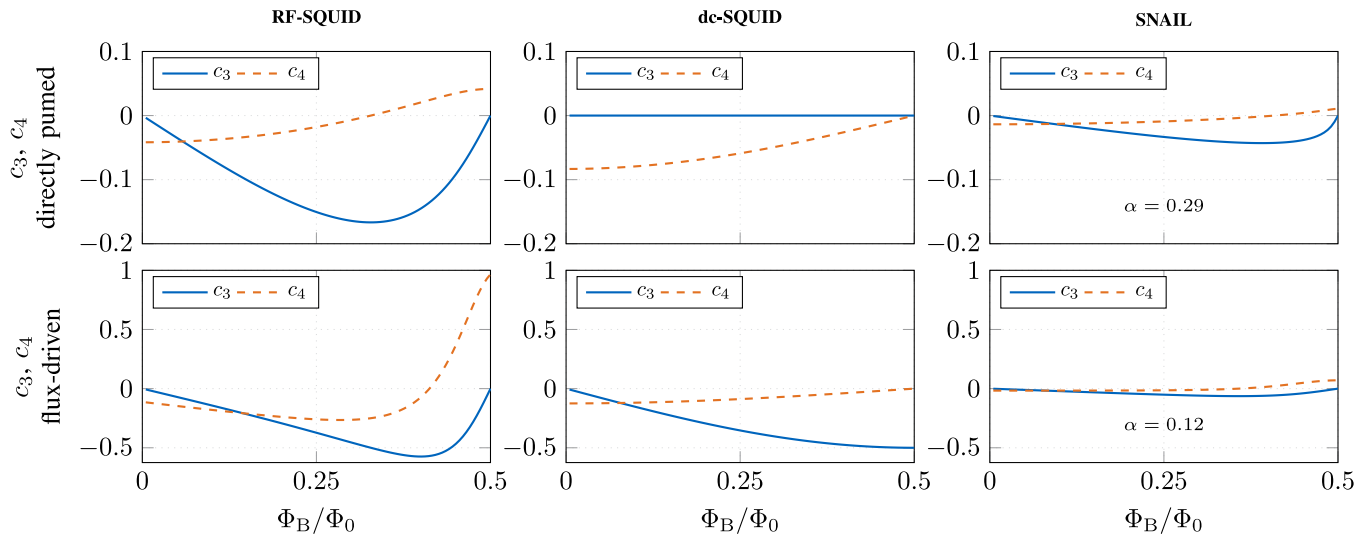

Fig. 5. Nonlinear coefficients c_3 and c_4 for an RF-SQUID (first column), a dc-SQUID (second column), and a SNAIL (third column). The upper row represents the nonlinear coefficients obtained for direct pumping, while the lower row represents the results for flux-driven nonlinear elements. The solid blue lines indicate the second-order nonlinear coefficient c_3, while the dashed orange lines represent the third-order Kerr-like coefficient c_4, respectively.

with $n \in \mathbb{N}$ and $|z| = 1$, instead. The solution for φ^* is then recovered via $\varphi^* = -in\log(z)$. For $n = 3$ large junctions, an analytic solution for φ^* can be obtained by solving a sixth-order polynomial equation for z. However, due to the double-well structure of the SNAIL, the minimum potential energy phase φ^* is not unique for large biases φ_B and large asymmetry ratios.

The coefficients c_2, c_3, and c_4 for the SNAIL are then given by

$$c_2 = \frac{1}{2}\left[\alpha\cos(\varphi^*) + \frac{1}{n}\cos\left(\frac{\varphi^* - \varphi_B}{n}\right)\right] \tag{81}$$

$$c_3 = \begin{cases} -\frac{1}{6}\left[\alpha\cos(\varphi^*) + \frac{1}{n^2}\cos\left(\frac{\varphi^* - \varphi_B}{n}\right)\right], & \text{for } m = 1 \\ \frac{1}{2}\frac{\mathrm{d}}{\mathrm{d}\varphi_{\text{ext}}}\left[\alpha\cos(\varphi^*) + \frac{1}{n^2}\cos\left(\frac{\varphi^* - \varphi_{\text{ext}}}{n}\right)\right]\Big|_{\varphi_{\text{ext}}=\varphi_B}, & \text{for } m = 0 \end{cases} \tag{82}$$

$$c_4 = \begin{cases} -\frac{1}{24}\left[\alpha\cos(\varphi^*) + \frac{1}{n^3}\cos\left(\frac{\varphi^* - \varphi_B}{n}\right)\right], & \text{for } m = 1 \\ \frac{1}{4}\frac{\mathrm{d}^2}{\mathrm{d}\varphi_{\text{ext}}^2}\left[\alpha\cos(\varphi^*) + \frac{1}{n^2}\cos\left(\frac{\varphi^* - \varphi_{\text{ext}}}{n}\right)\right]\Big|_{\varphi_{\text{ext}}=\varphi_B}, & \text{for } m = 0. \end{cases} \tag{83}$$

The second- and third-order nonlinear coefficients c_3 and c_4 for the RF-SQUID, the dc-SQUID, and the SNAIL are given in Fig. 5 for the case of direct pumping and external flux drive. It is apparent that a directly pumped dc-SQUID can only be operated in 4WM mode since the second-order nonlinear coefficient c_3 is uniformly zero for all bias points. The most significant nonlinear coefficients c_3 and c_4 are obtained for the RF-SQUID for both direct pumping and flux drive. However, it should be noted that the inverse linear inductance, given by the coefficient c_2, also plays an important role. The larger the nonlinear inductance, i.e., the smaller the coefficient c_2, the larger the 3WM and 4WM gains according to (50) and (51). We depict the inverse linear inductance for the RF-SQUID, the dc-SQUID, and the SNAIL in Fig. 6. The inverse linear inductance is the same for direct pumping and flux-driven TWPAs. Since we find different optimal asymmetry ratios α for the SNAIL for both pumping scenarios, we depict c_2 for the directly pumped SNAIL with $\alpha = 0.29$ and for the flux-driven SNAIL TWPA with $\alpha = 0.12$. The RF-SQUID and the dc-SQUID do not have any additional degrees of freedom. One can see in Fig. 6 that the flux-driven SNAIL-based TWPA (green) has by far the most significant inductance. Note here that a naïve optimization only accounting for the magnitudes of the second- and third-order nonlinear coefficients c_3 and c_4 favors an inferior design since the exact functional dependence of the inverse linear inductance parameter c_2, revealed by our black-box quantum model, must not be ignored.

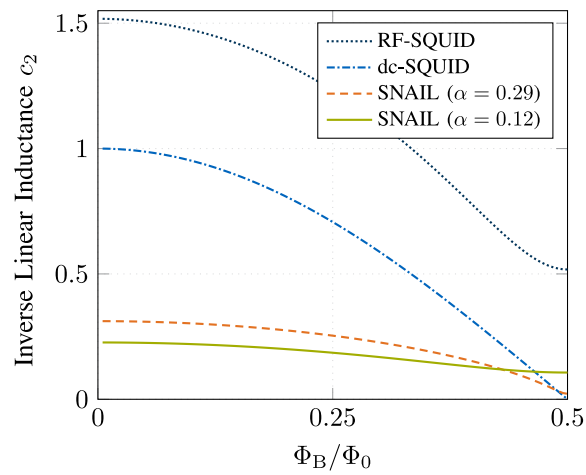

Fig. 6. Inverse linear inductance coefficient c_2 for an RF-SQUID (dotted, dark blue), a dc-SQUID (dashed–dotted, blue), a SNAIL with an asymmetry ratio of $\alpha = 0.29$ (dashed, orange), and a SNAIL with an asymmetry ratio of $\alpha = 0.12$ (solid, green).

VI. Conclusion

We have introduced a black-box quantum model for TWPAs based on nonlinear coefficients up to third order. The quantum model is based on a Hamiltonian that features all necessary effects, such as linear field propagation, 3WM, 4WM, SPM, and XPM, as well as losses and noise due to imperfect substrate isolation. The black-box model can accurately describe the gain and added quantum fluctuations for different nonlinear junction topologies. Using standard approximations, such as the rotating wave approximation, and assuming a strong undepleted classical pump, we found analytic solutions for the Heisenberg equations of motion for flux-driven and directly pumped TWPAs operating in 3WM and 4WM regimes. However, these approximations break down if the signal power becomes large, i.e., when it is close to the pump power. Hence, to describe further performance metrics, such as power handling capabilities in terms of gain compression, advanced numerical calculations beyond the analytical model presented here are necessary and shall be discussed in future work. For a single-junction 4WM TWPA, we were able to demonstrate excellent agreement of the results for the gain and added noise predicted by our analytical model with experimental results from the literature. The structure of the system Hamiltonian and insights from the analytic solutions were then used to find optimal working points for devices with different junction topologies, such as RF-SQUIDs, dc-SQUIDs, and SNAILs. We are confident that a systematic device synthesis approach using the black-box quantum model presented in this article will lead to new and better devices with optimized nonlinear elements for higher gain, larger bandwidth, and lower noise TWPAs.

Acknowledgment

The author would like to thank Y. Yuan for the stimulating discussions and her input on the unified notation for the wave-mixing Hamiltonians and J. Stowasser for proofreading the manuscript.

References

[1] F. Arute et al., "Quantum supremacy using a programmable superconducting processor," *Nature*, vol. 574, no. 7779, pp. 505–510, 2019.

[2] A. Morvan et al., "Phase transition in random circuit sampling," 2023, *arXiv:2304.11119*.

[3] L. Tosi, P. Rocca, N. Anselmi, and A. Massa, "Array-antenna power-pattern analysis through quantum computing," *IEEE Trans. Antennas Propag.*, vol. 71, no. 4, pp. 3251–3259, Apr. 2023.

[4] C. Ross, G. Gradoni, Q. J. Lim, and Z. Peng, "Engineering reflective metasurfaces with Ising Hamiltonian and quantum annealing," *IEEE Trans. Antennas Propag.*, vol. 70, no. 4, pp. 2841–2854, Apr. 2022.

[5] A. J. Daley et al., "Practical quantum advantage in quantum simulation," *Nature*, vol. 607, no. 7920, pp. 667–676, Jul. 2022.

[6] S. Bravyi, O. Dial, J. M. Gambetta, D. Gil, and Z. Nazario, "The future of quantum computing with superconducting qubits," *J. Appl. Phys.*, vol. 132, no. 16, Oct. 2022, Art. no. 160902.

[7] A. Blais, R.-S. Huang, A. Wallraff, S. M. Girvin, and R. J. Schoelkopf, "Cavity quantum electrodynamics for superconducting electrical circuits: An architecture for quantum computation," *Phys. Rev. A, Gen. Phys.*, vol. 69, Jun. 2004, Art. no. 062320.

[8] A. Wallraff et al., "Approaching unit visibility for control of a superconducting qubit with dispersive readout," *Phys. Rev. Lett.*, vol. 95, no. 6, Aug. 2005, Art. no. 060501.

[9] J. C. Bardin, D. H. Slichter, and D. J. Reilly, "Microwaves in quantum computing," *IEEE J. Microw.*, vol. 1, no. 1, pp. 403–427, Jan. 2021.

[10] M. D. Reed et al., "High-fidelity readout in circuit quantum electrodynamics using the Jaynes-Cummings nonlinearity," *Phys. Rev. Lett.*, vol. 105, no. 17, Oct. 2010, Art. no. 173601.

[11] J. Gambetta, W. A. Braff, A. Wallraff, S. M. Girvin, and R. J. Schoelkopf, "Protocols for optimal readout of qubits using a continuous quantum nondemolition measurement," *Phys. Rev. A, Gen. Phys.*, vol. 76, Jul. 2007, Art. no. 012325.

[12] C. M. Caves, "Quantum limits on noise in linear amplifiers," *Phys. Rev. D, Part. Fields*, vol. 26, pp. 1817–1839, Oct. 1982.

[13] B. Abdo, F. Schackert, M. Hatridge, C. Rigetti, and M. Devoret, "Josephson amplifier for qubit readout," *Appl. Phys. Lett.*, vol. 99, no. 16, Oct. 2011, Art. no. 162506.

[14] J. Aumentado, "Superconducting parametric amplifiers: The state of the art in Josephson parametric amplifiers," *IEEE Microw. Mag.*, vol. 21, no. 8, pp. 45–59, Aug. 2020.

[15] H. Zimmer, "Parametric amplification of microwaves in superconducting Josephson tunnel junctions," *Appl. Phys. Lett.*, vol. 10, no. 7, pp. 193–195, Apr. 1967.

[16] P. Russer, "Parametric amplification with Josephson junctions," *Arch. Elektr. Übertr.*, vol. 23, no. 8, pp. 417–420, 1969.

[17] W. Kaiser, M. Haider, J. A. Russer, P. Russer, and C. Jirauschek, "Quantum theory of the dissipative Josephson parametric amplifier," *Int. J. Circuit Theory Appl.*, vol. 45, no. 7, pp. 864–881, May 2017.

[18] G. Johansson, L. Tornberg, V. S. Shumeiko, and G. Wendin, "Readout methods and devices for Josephson-junction-based solid-state qubits," *J. Phys., Condens. Matter*, vol. 18, no. 21, pp. S901–S920, May 2006.

[19] G. Wendin and V. S. Shumeiko, "Quantum bits with Josephson junctions (review article)," *Low Temp. Phys.*, vol. 33, no. 9, pp. 724–744, Sep. 2007.

[20] F. Mallet et al., "Single-shot qubit readout in circuit quantum electrodynamics," *Nature Phys.*, vol. 5, no. 11, pp. 791–795, Sep. 2009.

[21] X. Gu, A. F. Kockum, A. Miranowicz, Y.-X. Liu, and F. Nori, "Microwave photonics with superconducting quantum circuits," *Phys. Rep.*, vols. 718–719, pp. 1–102, Nov. 2017.

[22] Y. Yuan, M. Haider, J. A. Russer, P. Russer, and C. Jirauschek, "Circuit quantum electrodynamic model of dissipative-dispersive Josephson traveling-wave parametric amplifiers," *Phys. Rev. A, Gen. Phys.*, vol. 107, Feb. 2023, Art. no. 022612.

[23] O. Yaakobi, L. Friedland, C. Macklin, and I. Siddiqi, "Parametric amplification in Josephson junction embedded transmission lines," *Phys. Rev. B, Condens. Matter*, vol. 87, no. 14, Apr. 2013, Art. no. 144301.

[24] K. O'Brien, C. Macklin, I. Siddiqi, and X. Zhang, "Resonant phase matching of Josephson junction traveling wave parametric amplifiers," *Phys. Rev. Lett.*, vol. 113, p. 157001, Oct. 2014.

[25] C. Macklin et al., "A near–quantum-limited Josephson traveling-wave parametric amplifier," *Science*, vol. 350, no. 6258, pp. 307–310, Oct. 2015.

[26] A. B. Zorin, "Josephson traveling-wave parametric amplifier with three-wave mixing," *Phys. Rev. Appl.*, vol. 6, Sep. 2016, Art. no. 034006.

[27] A. B. Zorin, "Flux-driven Josephson traveling-wave parametric amplifier," *Phys. Rev. Appl.*, vol. 12, Oct. 2019, Art. no. 044051.

[28] A. Miano et al., "Frequency-tunable Kerr-free three-wave mixing with a gradiometric SNAIL," *Appl. Phys. Lett.*, vol. 120, no. 18, May 2022.

[29] A. Blais, A. L. Grimsmo, S. M. Girvin, and A. Wallraff, "Circuit quantum electrodynamics," *Rev. Mod. Phys.*, vol. 93, May 2021, Art. no. 025005.

[30] V. V. Sivak, S. Shankar, G. Liu, J. Aumentado, and M. H. Devoret, "Josephson array-mode parametric amplifier," *Phys. Rev. Appl.*, vol. 13, Feb. 2020, Art. no. 024014.

[31] N. E. Frattini, U. Vool, S. Shankar, A. Narla, K. M. Sliwa, and M. H. Devoret, "3-wave mixing Josephson dipole element," *Appl. Phys. Lett.*, vol. 110, no. 22, May 2017, Art. no. 222603.

[32] R. A. Yusupov et al., "Flux-pumped Josephson travelling-wave parametric amplifiers based on Bi-SQUID cells," *IEEE Trans. Appl. Supercond.*, vol. 32, no. 4, pp. 1–5, Jun. 2022.

[33] L. Grönberg et al., "Side-wall spacer passivated sub-μm Josephson junction fabrication process," *Superconductor Sci. Technol.*, vol. 30, no. 12, Nov. 2017, Art. no. 125016.

[34] R. Kubo, "The fluctuation-dissipation theorem," *Rep. Prog. Phys.*, vol. 29, no. 1, pp. 255–284, Jan. 1966.

[35] M. Haider, Y. Yuan, and C. Jirauschek, "Including substrate losses and noise in a quantum mechanical model of a Josephson traveling-wave parametric amplifier," in *Proc. Int. Appl. Comput. Electromagn. Soc. Symp. (ACES)*, Aug. 2021, pp. 1–4.

[36] D. M. Pozar, *Microwave Engineering*, 4th ed. Hoboken, NJ, USA: Wiley, 2012.

[37] B. A. Kochetov and A. Fedorov, "The Lagrangian approach to a Josephson traveling-wave parametric amplifier," in *Proc. 8th Int. Conf. Ultrawideband Ultrashort Impulse Signals (UWBUSIS)*, Sep. 2016, pp. 112–116.

[38] H. R. Nilsson, A. F. Roudsari, D. Shiri, P. Delsing, and V. Shumeiko, "High-gain traveling-wave parametric amplifier based on three-wave mixing," *Phys. Rev. Appl.*, vol. 19, Apr. 2023, Art. no. 044056.

[39] A. Ranadive et al., "Kerr reversal in Josephson meta-material and traveling wave parametric amplification," *Nature Commun.*, vol. 13, no. 1, p. 1737, Apr. 2022.

[40] A. F. Roudsari et al., "Three-wave mixing traveling-wave parametric amplifier with periodic variation of the circuit parameters," *Appl. Phys. Lett.*, vol. 122, no. 5, Jan. 2023, Art. no. 052601.

[41] M. Haider, Y. Yuan, and C. Jirauschek, "Nonlinear elements in traveling-wave parametric amplifiers for dispersive qubit readout," in *Proc. 17th Eur. Conf. Antennas Propag. (EuCAP)*, Mar. 2023, pp. 1–5.

[42] M. Haider, Y. Yuan, J. A. Russer, and C. Jirauschek, "Quantum models for flux-driven superconducting traveling-wave parametric amplifiers with different nonlinear junction topologies," in *IEEE MTT-S Int. Microw. Symp. (IMS)*, San Diego, CA, Jun. 2023, pp. 664–667.

[43] A. Roy and M. Devoret, "Introduction to parametric amplification of quantum signals with Josephson circuits," *Comp. Rendus Phys.*, vol. 17, no. 7, pp. 740–755, Aug. 2016.

[44] U. Vool and M. Devoret, "Introduction to quantum electromagnetic circuits," *Int. J. Circuit Theory Appl.*, vol. 45, no. 7, pp. 897–934, Jun. 2017.

[45] M. O. Hecht, A. J. Cobarrubia, and K. M. Sundqvist, "An engineer's brief introduction to microwave quantum optics and a single-port state-space representation," *IEEE Trans. Quantum Eng.*, vol. 2, pp. 1–8, 2021.

[46] J. C. Bardin, D. Sank, O. Naaman, and E. Jeffrey, "Quantum computing: An introduction for microwave engineers," *IEEE Microw. Mag.*, vol. 21, no. 8, pp. 24–44, Aug. 2020.

[47] M. Sargent III, M. O. Scully, and W. E. J. Lamb, *Laser Physics*, 1st ed. Boston, MA, USA: Addison-Wesley Press, 1974.

[48] J. B. Johnson, "Thermal agitation of electricity in conductors," *Phys. Rev.*, vol. 32, pp. 97–109, Jul. 1928.

[49] H. Nyquist, "Thermal agitation of electric charge in conductors," *Phys. Rev.*, vol. 32, pp. 110–113, Jul. 1928.

[50] T. Van Der Reep, "Mesoscopic Hamiltonian for Josephson traveling-wave parametric amplifiers," *Phys. Rev. A, Gen. Phys.*, vol. 99, Jun. 2019, Art. no. 063838.

[51] M. Liscidini, L. G. Helt, and J. E. Sipe, "Asymptotic fields for a Hamiltonian treatment of nonlinear electromagnetic phenomena," *Phys. Rev. A, Gen. Phys.*, vol. 85, Jan. 2012, Art. no. 013833.

[52] A. L. Grimsmo and A. Blais, "Squeezing and quantum state engineering with Josephson travelling wave amplifiers," *Quantum Inf.*, vol. 3, no. 1, p. 20, Jun. 2017.

[53] N. Quesada and J. E. Sipe, "Effects of time ordering in quantum nonlinear optics," *Phys. Rev. A, Gen. Phys.*, vol. 90, Dec. 2014, Art. no. 063840.

[54] N. Quesada and J. E. Sipe, "Time-ordering effects in the generation of entangled photons using nonlinear optical processes," *Phys. Rev. Lett.*, vol. 114, Mar. 2015, Art. no. 093903.

[55] J. Manley and H. Rowe, "Some general properties of nonlinear elements—Part I. General energy relations," *Proc. IRE*, vol. 44, no. 7, pp. 904–913, Jul. 1956.

[56] P. Russer, "General energy relations for Josephson junctions," *Proc. IEEE*, vol. 59, no. 2, pp. 282–283, Feb. 1971.

[57] V. Weisskopf and E. Wigner, "Über die natürliche Linienbreite in der Strahlung des harmonischen Oszillators," *Z. Phys.*, vol. 65, pp. 18–29, Nov. 1930.

[58] M. Houde, L. C. G. Govia, and A. A. Clerk, "Loss asymmetries in quantum traveling-wave parametric amplifiers," *Phys. Rev. Appl.*, vol. 12, Sep. 2019, Art. no. 034054.

[59] K. Peng, M. Naghiloo, J. Wang, G. D. Cunningham, Y. Ye, and K. P. O'Brien, "Floquet-mode traveling-wave parametric amplifiers," *PRX Quantum*, vol. 3, Apr. 2022, Art. no. 020306.

[60] S. Simbierowicz et al., "Characterizing cryogenic amplifiers with a matched temperature-variable noise source," *Rev. Sci. Instrum.*, vol. 92, no. 3, Mar. 2021, Art. no. 034708.

[61] S. Zhao and S. Withington, "Quantum analysis of second-order effects in superconducting travelling-wave parametric amplifiers," *J. Phys. D, Appl. Phys.*, vol. 54, no. 36, Jun. 2021, Art. no. 365303.

[62] L. Fasolo et al., "Bimodal approach for noise figures of merit evaluation in quantum-limited Josephson traveling wave parametric amplifiers," *IEEE Trans. Appl. Supercond.*, vol. 32, no. 4, pp. 1–6, Jun. 2022.

Michael Haider (Member, IEEE) received the B.Sc., M.Sc., and Ph.D. (summa cum laude) degrees in electrical and computer engineering from the Technical University of Munich (TUM), Garching, Germany, in 2014, 2016, and 2019, respectively.

From 2016 to 2019, he was a Research Associate with the Institute of Nanoelectronics, TUM, where his research focused on quantum circuit theory, wireless power transfer, and stochastic electromagnetic fields. In 2019, he joined the Computational Photonics Group, TUM, as a Post-Doctoral Researcher, where he became a permanent staff Scientist in October 2023. He has coauthored over 100 scientific papers in refereed journals and conference proceedings. His current research interests include the modeling of charge carrier transport in quantum cascade lasers, the dynamical modeling of quantum devices within a generalized Maxwell-Bloch framework, and quantum circuit theoretical models applied to Josephson traveling-wave parametric amplifiers.

Dr. Haider received the 2020 VDE ITG Dissertationspreis for his outstanding Ph.D. thesis on Investigations of Stochastic Electromagnetic Fields.